

## Balanced and Unbalanced Components of Moist Atmospheric Flows with Phase Changes\*

Alfredo N. WETZEL<sup>1</sup>      Leslie M. SMITH<sup>2</sup>  
Samuel N. STECHMANN<sup>3</sup>      Jonathan E. MARTIN<sup>4</sup>

*Dedicated to Professor Andrew J. Majda on the occasion of his 70th birthday*

**Abstract** Atmospheric variables (temperature, velocity, etc.) are often decomposed into balanced and unbalanced components that represent low-frequency and high-frequency waves, respectively. Such decompositions can be defined, for instance, in terms of eigenmodes of a linear operator. Traditionally these decompositions ignore phase changes of water since phase changes create a piecewise-linear operator that differs in different phases (cloudy versus non-cloudy). Here we investigate the following question: How can a balanced–unbalanced decomposition be performed in the presence of phase changes? A method is described here motivated by the case of small Froude and Rossby numbers, in which case the asymptotic limit yields precipitating quasi-geostrophic equations with phase changes. Facilitated by its zero-frequency eigenvalue, the balanced component can be found by potential vorticity (PV) inversion, by solving an elliptic partial differential equation (PDE), which includes Heaviside discontinuities due to phase changes. The method is also compared with two simpler methods: one which neglects phase changes, and one which simply treats the raw pressure data as a streamfunction. Tests are shown for both synthetic, idealized data and data from Weather Research and Forecasting (WRF) model simulations. In comparisons, the phase-change method and no-phase-change method produce substantial differences within cloudy regions, of approximately 5 K in potential temperature, due to the presence of clouds and phase changes in the data. A theoretical justification is also derived in the form of a elliptic PDE for the differences in the two streamfunctions.

**Keywords** Potential vorticity inversion, Moist atmospheric dynamics, Slow-fast systems, Balanced-unbalanced decomposition, Elliptic partial differential equations

**2000 MR Subject Classification** 35R05, 86A10

---

Manuscript received April 30, 2019.

<sup>1</sup>Department of Mathematics, University of Wisconsin-Madison, Madison, WI 53706, USA.

E-mail: alfredo.wetzel@wisc.edu

<sup>2</sup>Department of Mathematics and Department of Engineering Physics, University of Wisconsin-Madison, Madison, WI 53706, USA. E-mail: lsmith@math.wisc.edu

<sup>3</sup>Department of Mathematics and Department of Atmospheric and Oceanic Sciences, University of Wisconsin-Madison, Madison, WI 53706, USA. E-mail: stechmann@wisc.edu

<sup>4</sup>Department of Atmospheric and Oceanic Sciences, University of Wisconsin-Madison, Madison, WI 53706, USA.

E-mail: jemarti1@wisc.edu

\*This work was supported by the National Science Foundation through grant AGS-1443325 and DMS-1907667 and the University of Wisconsin-Madison Office of the Vice Chancellor for Research and Graduate Education with funding from the Wisconsin Alumni Research Foundation.

## 1 Introduction

It is often desirable to decompose atmospheric variables (temperature, velocity, etc.) into balanced and unbalanced components. Here, the terms balanced and unbalanced are used to refer to low-frequency and high-frequency components, respectively, which evolve on slow and fast time scales, respectively. The balanced component is typically associated with a scalar variable, called potential vorticity (PV), or a quasi-geostrophic (QG) PV that arises approximately in an asymptotic limit. The ideas of balance and PV have been widely used and beneficial in contexts such as, for instance, analyzing atmospheric dynamics (see, e.g., [13, 21, 36] and references therein) and data assimilation and forecasting (see, e.g., [2, 14, 20, 32, 39] and references therein). Furthermore, rigorous mathematical theory, such as fast-wave averaging, can be proved for balanced–unbalanced decompositions [7, 8, 30, 31].

Traditionally, balanced–unbalanced decompositions are based on *dry* dynamics of the atmosphere, without consideration of moisture or phase changes of water between, e.g., vapor and liquid phases. If phase changes of water are present, then one needs to define variables (such as PV) that appropriately account for water and its phase changes. Alternatively, from a related point of view, eigenmodes can be taken as the quantity of interest instead of PV, since PV can be associated with a low-frequency eigenmode (the vortical mode) of the linear operator  $\mathcal{L}$  of the atmospheric fluid dynamics equations. In particular, in the case of dry dynamics, the fluid dynamics equations can be written abstractly as

$$\frac{\partial \mathbf{v}}{\partial t} + \epsilon^{-1} \mathcal{L}(\mathbf{v}) + \mathcal{B}(\mathbf{v}, \mathbf{v}) = 0, \quad (1.1)$$

where  $\mathcal{L}$  is a linear operator,  $\epsilon$  is a small number (related to Froude and/or Rossby numbers),  $\mathcal{B}$  is a bilinear operator, and  $\mathbf{v}$  is a vector of all fluid dynamics variables (temperature, velocity, etc.) [30]. When phase changes are present, the linear operator  $\mathcal{L}$  becomes a piecewise linear operator  $H_u \mathcal{L}_u + H_s \mathcal{L}_s$  that takes a different form in cloudy versus non-cloudy regions:

$$\frac{\partial \mathbf{v}}{\partial t} + \epsilon^{-1} (H_u \mathcal{L}_u(\mathbf{v}) + H_s \mathcal{L}_s(\mathbf{v})) + \mathcal{B}(\mathbf{v}, \mathbf{v}) = 0, \quad (1.2)$$

where  $H_u$  and  $H_s$  are Heaviside functions that indicate unsaturated and saturated phases, respectively. In this case with phase changes, it is unclear how to best perform a decomposition into balanced and unbalanced components for the piecewise linear operator.

The main purpose of the present paper is to investigate the question: How can a balanced–unbalanced decomposition be performed in the presence of phase changes? While one could formulate the methods in a setting of any Froude and Rossby numbers (i.e., any value of  $\epsilon$  in (1.1)–(1.2)), the main methods that are proposed and tested here will use the simplifying assumption of small Froude and Rossby numbers (although also tested for their applicability in general settings where Froude and Rossby numbers are not necessarily small). The theoretical assumption of small Froude and Rossby numbers allows the use of a QG PV variable, in which case the identification of the balanced component is somewhat simplified. The balanced

component can be found by solving an elliptic partial differential equation (PDE), and the process of solving this elliptic PDE is known as PV inversion. Here, we are motivated by a new version of QG equations and PV inversion that includes moisture, precipitation, and phase changes of water. These precipitating quasi-geostrophic (PQG) equations were recently derived as the asymptotic limit, for small (moist) Froude and Rossby numbers, of an atmosphere with moisture and phase changes [43].

Other methods for moist PV inversion have been proposed in the past (e.g., [37, 41, 50]), and they differ from [43] and the present paper in some fundamental ways. One of the most distinguishing aspects of [43] is in its recognition that, if moisture is present, then the balanced component of the flow is a two-dimensional space, rather than a one-dimensional space characterized by only the single PV variable. A second balanced variable, called  $M$  due to its association with moisture, is used by [43] to complete the specification of the two-dimensional balanced component. From an eigenmode perspective, the addition of a moisture variable creates a new eigenmode that is not present in dry dynamics, and the new eigenmode can be associated with the variable  $M$ . As a result, for moist dynamics, the balanced component is obtained by the process of PV-and- $M$  inversion, rather than dry PV inversion.

This article is dedicated to Andrew J. Majda to celebrate his 70th birthday, and it has drawn on his influence through his many contributions to topics of, e.g., balanced dynamics, singular limits, and fast-wave averaging for fluids with small Mach, Froude, and/or Rossby numbers [3, 4, 5, 7, 8, 17, 18, 29, 30, 31, 33], and PDEs and atmospheric dynamics with nonlinear switches [10, 16, 34, 44].

This paper is organized as follows. In Section 2, we describe how to construct the balanced components of atmospheric variables. We begin by describing the motivating model, the PQG equations with three moisture constituents and their derivation in the QG limit from the anelastic equations. We then describe some aspects associated with the inversion of PV and  $M$  to recover the streamfunction. In Section 3, we discuss three different methods that may be employed to recover the balanced streamfunction. We finish that section by discussing the simple numerical method that we use to invert the PV. In Section 4, we use the inversion methods of Section 3 to discuss the effects of a simple, idealized PV and  $M$  with phase transitions on the balanced streamfunction and temperature. Lastly, in Section 5, we use the inversion methods on simulated data for a mid-latitude simulation of a channel flow. We then discuss the balanced streamfunction, velocity, and temperature and the effect that the moisture has on their structure.

## 2 Model Motivation: The Quasi-Geostrophic Limit of the Precipitating Anelastic Equations

Here, we use the PQG equations to motivate the decomposition of a moist atmospheric model into balanced (zero-frequency or vortical) and unbalanced (high-frequency or wave) components.

Specifically, the potential vorticity as defined in the QG sense will give a natural decomposition of the system into balanced (zero-frequency) and unbalanced (high-frequency) contributions by filtering out of high-frequency modes. The fact that moisture is included in our starting set of anelastic equations means that these moist QG equations will include zero-frequency or low-frequency modes associated with moisture contributions.

We begin by describing the anelastic equations of moist air with three phases of water (water vapor, cloud water, and rainwater) in Section 2.1. We then discuss the derivation of the system in the quasi-geostrophic limit in Section 2.2. This asymptotic limit gives rise to what are called the PQG equations. We finish the section by briefly discussing how a balanced or low-frequency mode is determined for the total water of the system in Section 2.3.

## 2.1 Anelastic equations with three moisture constituents

Our starting point are the governing anelastic equations for moist air with three water constituents [1, 11, 26, 38]:

$$\frac{D\mathbf{u}}{Dt} + f\hat{\mathbf{z}} \times \mathbf{u} = -\nabla\left(\frac{p}{\tilde{\rho}}\right) + \hat{\mathbf{z}}b, \quad (2.1a)$$

$$\nabla \cdot (\tilde{\rho}\mathbf{u}) = 0, \quad (2.1b)$$

$$\frac{D\theta}{Dt} + w\frac{d\tilde{\theta}}{dz} = \frac{L_v}{c_p}\frac{\tilde{\theta}}{\tilde{T}}(C_d - E_r), \quad (2.1c)$$

$$\frac{Dq_v}{Dt} + w\frac{d\tilde{q}_v}{dz} = -C_d + E_r, \quad (2.1d)$$

$$\frac{Dq_c}{Dt} = C_d - A_r - C_r, \quad (2.1e)$$

$$\frac{Dq_r}{Dt} - \frac{1}{\tilde{\rho}}\frac{\partial}{\partial z}(\tilde{\rho}V_Tq_r) = A_r + C_r - E_r. \quad (2.1f)$$

Here  $\mathbf{u} = (u, v, w)$  is the velocity vector, where  $u$  is the zonal (west-east),  $v$  is the meridional (south-north), and  $w$  is the vertical (down-up) velocity component;  $\rho$  is the density;  $p$  is the pressure;  $T$  is the temperature;  $\theta$  is the potential temperature;  $q_v$  is the water vapor mixing ratio;  $q_c$  is the cloud water mixing ratio; and  $q_r$  is the rainwater mixing ratio. The buoyancy  $b = b(\theta, q_v, q_c, q_r)$  is given by the formula

$$b = g\left(\frac{\theta}{\tilde{\theta}} + \varepsilon_0q_v - q_c - q_r\right). \quad (2.1g)$$

The material derivative operator is defined as  $D/Dt := \partial/\partial t + \mathbf{u} \cdot \nabla$  with  $\nabla := (\partial/\partial x, \partial/\partial y, \partial/\partial z)$  being the gradient operator and  $\hat{\mathbf{z}}$  is a unit vector in the direction of gravity. The thermodynamic variables  $\rho$ ,  $p$ ,  $\theta$ ,  $T$  and moisture variables  $q_v$ ,  $q_c$ ,  $q_r$  have been decomposed such that

the static background states, denoted by a tilde  $\widetilde{(\cdot)}$ , are functions of the height  $z$  only, e.g., the total potential temperature is given by  $\widetilde{\theta}(z) + \theta(x, y, z, t)$  with anelastic background state  $\widetilde{\theta}$  and anomaly/perturbation  $\theta$ . The static background states are freely chosen to match an atmospheric state of interest; for this paper we choose a hydrostatically balanced pressure and density and  $\widetilde{q}_c = \widetilde{q}_r = 0$ . Lastly,  $g$  is the acceleration due to gravity,  $f$  is the constant Coriolis parameter,  $L_v$  is the latent heat factor,  $c_p$  is the specific heat at constant pressure,  $\varepsilon_0 = R_v/R_d - 1$  is the ratio of water vapor  $R_v$  and dry air  $R_d$  gas constants, and  $V_T$  is the rainfall speed, which is assumed to be constant for simplicity.

The source terms in prognostic equations (2.1c)–(2.1f) allow for the conversion between moisture constituents  $q_v$ ,  $q_c$ ,  $q_r$  and correspond to the following moist thermodynamic processes:  $C_d$  symbolizes the condensation of water vapor to form cloud water,  $E_r$  is the evaporation of rainwater into water vapor,  $A_r$  is the auto-conversion of cloud water into rainwater, and  $C_r$  is the collection of cloud water to form rainwater. A complete characterization of these source terms requires modeling the microphysics and the thermodynamic properties of the system (e.g., [15]) beyond the scope of the present paper. The cloud condensation term  $C_d$ , however, may be defined implicitly so as to impose the condition that (i) there is no cloud water in unsaturated regions and (ii) the water vapor is at saturation in regions with cloud water [11]. Indeed, the condensation term implies the following conditions of moisture must be satisfied in saturated and unsaturated regions:

$$q_v < q_{vs}, \quad q_c = 0 \quad (\text{unsaturated}), \quad (2.2a)$$

$$q_v = q_{vs}, \quad q_c \geq 0 \quad (\text{saturated}), \quad (2.2b)$$

where  $q_{vs}$  is the water vapor at saturation. In principle, the saturation water vapor  $q_{vs}$  depends on the pressure and temperature of the system [40]. For simplicity, however, here  $q_{vs}$  denotes a prescribed water vapor saturation profile that depends on the height only, i.e.,  $q_{vs} = q_{vs}(z)$  [12, 19]. While conditions (2.2a)–(2.2b) do not allow for supersaturation of water vapor in saturated regions, water vapor is immediately relaxed to its saturation value  $q_v = q_{vs}$  in saturated regions, the conditions impose no constraint on the rainwater. Thus, both unsaturated and saturated regions permit rainwater.

Phase conditions (2.2a)–(2.2b) allow us to reduce the number of thermodynamic evolution equations (2.1c)–(2.1f) from four to three. Specifically, the total water mixing ratio  $q_t = q_v + q_c + q_r$  and the rainwater mixing ratio  $q_r$  are now sufficient to determine all moisture constituents  $q_v$ ,  $q_c$ ,  $q_r$ . To see this fact, phase conditions (2.2a)–(2.2b) may be written in the form

$$q_t - q_r < q_{vs}, \quad q_c = 0 \quad (\text{unsaturated}), \quad (2.3a)$$

$$q_t - q_r \geq q_{vs}, \quad q_v = q_{vs} \quad (\text{saturated}). \quad (2.3b)$$

These conditions, in turn, may be used to deduce the formulas

$$q_v = \min(q_t - q_r, q_{vs}), \quad (2.4a)$$

$$q_c = \max(0, q_t - q_r - q_{vs}). \quad (2.4b)$$

It is customary to then write the thermodynamic equations of the system in terms of the equivalent potential temperature  $\theta_e$  and total water  $q_t$  [6, 45]. The variables  $\theta_e$  and  $q_t$  have the advantage that their evolution equations do not include the source terms  $C_d$ ,  $E_r$ ,  $A_r$ , or  $C_r$ . Additionally, we supplement the equations for  $\theta_e$  and  $q_t$  with an equation for the rainwater  $q_r$ . Thus, the 4 thermodynamic equations (2.1c)–(2.1f) may be reduced to the thermodynamic equations [6, 43, 45]

$$\frac{D\theta_e}{Dt} + w \frac{d\tilde{\theta}_e}{dz} = 0, \quad (2.5a)$$

$$\frac{Dq_t}{Dt} + w \frac{d\tilde{q}_t}{dz} - \frac{1}{\tilde{\rho}} \frac{\partial}{\partial z} (\tilde{\rho} V_T q_r) = 0, \quad (2.5b)$$

$$\frac{Dq_r}{Dt} - \frac{1}{\tilde{\rho}} \frac{\partial}{\partial z} (\tilde{\rho} V_T q_r) = A_r + C_r - E_r. \quad (2.5c)$$

For our purposes, thermodynamic and moisture variables are related by means of the linearized equivalent potential temperature equations for the background and anomaly:

$$\frac{d\tilde{\theta}_e}{dz} = \frac{d\tilde{\theta}}{dz} + \frac{L_v}{c_p \tilde{\Pi}} \frac{d\tilde{q}_v}{dz} \quad \text{and} \quad \theta_e = \theta + \frac{L_v}{c_p \tilde{\Pi}} q_v, \quad (2.6a)$$

where  $\tilde{\Pi} = \tilde{T}/\tilde{\theta} = (\tilde{p}/p_0)^{R_d/c_p}$  is the Exner function for the background pressure and  $p_0$  is the surface pressure reference state. Lastly, the background and anomaly total water  $q_t$  are given by:

$$\tilde{q}_t = \tilde{q}_v \quad \text{and} \quad q_t = q_v + q_c + q_r. \quad (2.6b)$$

In addition, we assume that  $\tilde{q}_{vs} = \tilde{q}_v$  so that both the total moisture variables, e.g.,  $\tilde{q}_t + q_t$ , and moisture anomalies satisfy conditions (2.2a)–(2.3b).

The anelastic evolution equations with three moisture constituents may then be taken to consist of the two equations (2.1a)–(2.1b) and three thermodynamic equations (2.5a)–(2.5c).

## 2.2 Quasi-Geostrophic anelastic equations with three moisture constituents

In what follows, we use the anelastic equations presented in the previous section to derive the anelastic PQG equations. We attempt to highlight key features of this procedure and refer the interested reader to [43] for details on the asymptotic derivation.

The quasi-geostrophic limit entails an asymptotic scaling of comparable and small Rossby and Froude numbers. Additionally, due to the thermodynamic equations (2.5a)–(2.5b), we must specify the relative size of the background states  $d\tilde{\theta}_e/dz$  and  $d\tilde{q}_t/dz$ . We assume that the background states  $d\tilde{\theta}_e/dz$  and  $(L_v/c_p)d\tilde{q}_t/dz$  are comparable and large in relation to the Rossby number. Specifically, these terms are large enough to balance the horizontal advection of the  $\theta_e$  and  $q_t$  anomalies in equations (2.5a)–(2.5b). Under these assumptions, the leading order balance in the system of equations (2.1a)–(2.1b) with (2.5a)–(2.5c) consists of geostrophic balance for horizontal motions and hydrostatic balance for vertical motions. This leading order balance naturally gives rise to a streamfunction  $\psi$  satisfying

$$b = f \frac{\partial \psi}{\partial z}, \quad (2.7a)$$

$$\mathbf{u}_H = \left( -\frac{\partial \psi}{\partial y}, \frac{\partial \psi}{\partial x} \right), \quad (2.7b)$$

$$\zeta = \nabla_H^2 \psi, \quad (2.7c)$$

where  $\psi = p/(f\tilde{\rho})$ ,  $\mathbf{u}_H = (u, v)$  is the horizontal velocity vector, and  $\zeta$  is the relative vorticity with  $\nabla_H^2 := \partial^2/\partial x^2 + \partial^2/\partial y^2$  being the horizontal Laplacian. The vertical velocity does not appear in the above set of equations as it is identically zero at this order. Moreover, at leading order, explicit moisture contributions from  $q_v$ ,  $q_c$ ,  $q_r$  to the buoyancy (2.1g) vanish [43, 49] and the buoyancy in the quasi-geostrophic limit is given by

$$b = g \frac{\theta}{\tilde{\theta}}; \quad (2.7d)$$

resembling in form the buoyancy obtained in dry quasi-geostrophic dynamics (e.g., [48]). Implicitly, however, the buoyancy (2.7d) still retains important moisture information by means of the phase transitions of the system.

The anelastic PQG equations with three moisture constituents are then [43]

$$\frac{D_H \zeta}{Dt} = \frac{f}{\tilde{\rho}} \frac{\partial}{\partial z} (\tilde{\rho} w), \quad (2.8a)$$

$$\frac{D_H \theta_e}{Dt} + w \frac{d\tilde{\theta}_e}{dz} = 0, \quad (2.8b)$$

$$\frac{D_H q_t}{Dt} + w \frac{d\tilde{q}_t}{dz} = \frac{1}{\tilde{\rho}} \frac{\partial}{\partial z} (\tilde{\rho} V_T q_r), \quad (2.8c)$$

$$\frac{D_H q_r}{Dt} = \frac{1}{\tilde{\rho}} \frac{\partial}{\partial z} (\tilde{\rho} V_T q_r) + A_r + C_r - E_r. \quad (2.8d)$$

The horizontal material derivative operator  $D_H/Dt$  is defined in the expected manner by  $D_H/Dt := \partial/\partial t + \mathbf{u}_H \cdot \nabla_H$  with the horizontal gradient  $\nabla_H := (\partial/\partial x, \partial/\partial y)$ .

In addition, the PQG equations (2.8a)–(2.8d) may be combined so as to eliminate the vertical velocity variable  $w$ ; much like in dry QG [48]. These new equations naturally define a potential vorticity variable, denoted the equivalent potential vorticity  $PV_e$ , and two additional variables due to the moisture constituents  $q_t$  and  $q_r$  [43]. These new variables take the form

$$PV_e = \zeta + \frac{f}{\tilde{\rho}} \frac{\partial}{\partial z} \left( \frac{\tilde{\rho}}{d\tilde{\theta}_e/dz} \theta_e \right), \quad (2.9a)$$

$$M = q_t + G_M \theta_e, \quad (2.9b)$$

$$M_r = M - q_r \quad (2.9c)$$

with evolution equations

$$\frac{D_H PV_e}{Dt} = -\frac{f}{d\tilde{\theta}_e/dz} \frac{\partial \mathbf{u}_H}{\partial z} \cdot \nabla_H \theta_e, \quad (2.10a)$$

$$\frac{D_H M}{Dt} = \frac{1}{\tilde{\rho}} \frac{\partial}{\partial z} (\tilde{\rho} V_T q_r), \quad (2.10b)$$

$$\frac{D_H M_r}{Dt} = E_r - A_r - C_r, \quad (2.10c)$$

where  $G_M = -(d\tilde{q}_t/dz)/(d\tilde{\theta}_e/dz)$  is a function of  $z$ .

In complete analogy with dry QG, it is natural to attempt to formulate a diagnostic equation for the streamfunction  $\psi$  in terms of the dynamic variables  $PV_e$ ,  $M$ , and  $M_r$ . In this way, we may derive an inversion procedure for the streamfunction  $\psi$  in terms of the potential vorticity and moisture variables of PQG. Since  $PV_e$ ,  $M$ , and  $M_r$  correspond to low-frequency or balanced variables by construction, we use these variables as a starting point to define all balanced components of the system. Namely, as we proceed to describe below, from the variables  $PV_e$ ,  $M$ , and  $M_r$  we determine the balanced streamfunction  $\psi$ , which may then be used to obtain all other balanced variables.

To construct the inversion for  $\psi$ , we use the equivalent potential vorticity equation (2.9a) and write down both  $\zeta$  and  $\theta_e$  in terms of  $\psi$ ,  $M$ , and/or  $M_r$ . The relative vorticity  $\zeta$  is directly related to the streamfunction  $\psi$  by equation (2.7c). The equivalent potential temperature  $\theta_e$ , however, requires more discussion. In the quasi-geostrophic limit, equation (2.6a) for  $\theta_e$  remains unchanged. Therefore, using the fact that (2.4a) can be written in the form  $q_v = (q_t - q_r)H_u + q_{vs}H_s$ , we use equation (2.6a) to write down an equation for  $\theta_e$  in terms of  $\theta$  and  $M_r$  in both the saturated and unsaturated regions, where

$$H_u = \begin{cases} 1 & \text{if } q_t - q_r < q_{vs} \quad (\text{unsaturated}) \\ 0 & \text{if } q_t - q_r \geq q_{vs} \quad (\text{saturated}) \end{cases} \quad \text{and} \quad H_s = 1 - H_u \quad (2.11)$$

are the indicator functions for the unsaturated or saturated regions. Specifically, using (2.9b)–(2.9c), equation (2.6a) for  $\theta_e$  becomes

$$\theta_e = \left( \theta + \frac{L_v}{c_p \tilde{\Pi}} (M_r - G_M \theta_e) \right) H_u + \left( \theta + \frac{L_v}{c_p \tilde{\Pi}} q_{vs} \right) H_s \quad (2.12a)$$

or solving for  $\theta_e = \theta_e(\theta, M_r, z)$  and using the background  $\tilde{\theta}_e$  equation (2.6a) we obtain

$$\frac{1}{d\tilde{\theta}_e/dz} \theta_e = \frac{g}{\tilde{\theta}} \frac{1}{N_u^2} \left( \theta + \frac{L_v}{c_p \tilde{\Pi}} M_r \right) H_u + \frac{g}{\tilde{\theta}} \frac{1}{N_s^2} \left( \theta + \frac{L_v}{c_p \tilde{\Pi}} q_{vs} \right) H_s, \quad (2.12b)$$

where we define the buoyancy frequencies

$$N_u^2 = \frac{g}{\tilde{\theta}} \frac{d\tilde{\theta}}{dz} \quad \text{and} \quad N_s^2 = \frac{g}{\tilde{\theta}} \frac{d\tilde{\theta}_e}{dz}. \quad (2.13)$$

Then, using (2.12b), the potential vorticity equation (2.9a) becomes

$$PV_e = \zeta + \frac{f}{\tilde{\rho}} \frac{\partial}{\partial z} \left( \tilde{\rho} \frac{g}{\tilde{\theta}} \frac{1}{N_u^2} \left( \theta + \frac{L_v}{c_p \tilde{\Pi}} M_r \right) H_u + \tilde{\rho} \frac{g}{\tilde{\theta}} \frac{1}{N_s^2} \left( \theta + \frac{L_v}{c_p \tilde{\Pi}} q_{vs} \right) H_s \right). \quad (2.14a)$$

We may then use (2.7a)–(2.7d) on (2.14a) to obtain the inversion relation for  $\psi$  in terms of  $PV_e$  and  $M_r$ :

$$\nabla_H^2 \psi + \frac{1}{\tilde{\rho}} \frac{\partial}{\partial z} \left( \tilde{\rho} \frac{f^2}{N^2} \frac{\partial \psi}{\partial z} \right) = PV_e - \frac{1}{\tilde{\rho}} \frac{\partial}{\partial z} \left( \tilde{\rho} \frac{g}{f \tilde{\theta}} \frac{L_v}{c_p \tilde{\Pi}} \frac{f^2}{N^2} (M_r H_u + q_{vs} H_s) \right), \quad (2.14b)$$

where

$$N^2 = N_u^2 H_u + N_s^2 H_s. \quad (2.15)$$

For PQG, the balanced streamfunction  $\psi$  can then be found by solving the nonlinear, non-constant coefficient, elliptic partial differential equation (2.14b) using suitable boundary conditions. It is worth noting that the three moisture constituent inversion (2.14b) requires knowledge not only of the potential vorticity variable, as in dry QG, but also of a moisture variable in the form of  $M_r$ . This is in complete analogy to the two moisture constituent inversion presented in [43], where the moisture variable needed was  $M$  rather than  $M_r$ . Recall that here  $q_{vs}$  is assumed to be prescribed and therefore does not feature as part of the variables of the system.

Moreover, for PQG, the nonlinearity in inversion (2.14b) arises from the indicator functions  $H_u$  and  $H_s$  due to the fact that they depend implicitly on the streamfunction. To highlight this fact, note that we may write the phase transition conditions (2.11) in terms of  $\psi$ ,  $PV_e$ ,  $M$ , and/or  $M_r$  as follows. First, using (2.9b)–(2.9c) we may simply write  $q_t - q_r$  as

$$q_t - q_r = M_r - G_M \theta_e. \quad (2.16)$$

Second, using the fact that  $\theta_e$  is given by (2.6a) and  $q_v = (q_t - q_r)H_u + q_{vs}H_s$  by (2.4a), we may gather terms and write

$$(q_t - q_r)(D_M H_u + H_s) = M_r - G_M \theta + (1 - D_M) q_{vs} H_s, \quad (2.17)$$

where equations (2.13) and the definition of the background state  $\tilde{\theta}_e$  in (2.6a) allow us to define

$$D_M = 1 + G_M \frac{L_v}{c_p \tilde{\Pi}} = \frac{N_u^2}{N_s^2}. \quad (2.18)$$

Lastly, subtracting  $q_{vs}(D_M H_u + H_s)$  from both sides in (2.17) gives

$$(q_t - q_r - q_{vs})(D_M H_u + H_s) = M_r - G_M \theta - D_M q_{vs}. \quad (2.19)$$

Since  $D_M H_u + H_s \geq 0$  by definition, equation (2.19) shows that we may equally take the sign of  $M_r - G_M \theta - D_M q_{vs}$  or  $q_t - q_r - q_{vs}$  as our condition to determine phase transitions. Specifically, this means that we may re-write the indicator function  $H_u$  in terms of the variables  $M_r$  and  $\psi$  (the potential temperature  $\theta$  is related to only  $\psi$  by (2.7a) and (2.7d)) as

$$H_u = \begin{cases} 1 & \text{if } M_r - G_M \theta < D_M q_{vs} \quad (\text{unsaturated}) \\ 0 & \text{if } M_r - G_M \theta \geq D_M q_{vs} \quad (\text{saturated}) \end{cases} \quad \text{and} \quad H_s = 1 - H_u. \quad (2.20)$$

We note in passing that it is peculiar that the moisture variable  $M$  is not required for the inversion (2.14b), the determination of the phase boundaries (2.20), and the computation of water vapor  $q_v$  and cloud water  $q_c$  by means of the equations (2.4a)–(2.4b) and (2.17). One may legitimately ask the question whether  $M$  is a necessary variable in the system or whether one may dismiss this variable. The variable  $M$  is indeed necessary to determine  $q_t$  and  $q_r$ , as we show in Section 2.3; these variables being most likely required to determine the source terms  $A_r$ ,  $C_r$ ,  $E_r$  in equation (2.10c) for the evolution of  $M_r$ .

In summary, the balanced or low-frequency component of the streamfunction can be found by solving (2.14b) for known  $PV_e$  and  $M_r$ . Other balanced components can be found using this balanced streamfunction and the variables  $PV_e$ ,  $M$ , and  $M_r$ . Specifically, the balanced horizontal velocity is obtained directly from (2.7b) and the balanced potential temperature is obtained from (2.7a)–(2.7d). To obtain a balanced component for the moisture variables of the system is more involved. We describe such a process for total water anomaly  $q_t$  in the next subsection.

### 2.3 Balanced component of total water

To find the balanced component of total water, we write down the equation for  $q_t$  in terms of the balanced variables  $\psi$ ,  $PV_e$ ,  $M$ , and/or  $M_r$ . This procedure will be analogous to that discussed to obtain (2.17) in the previous section. We begin by using (2.9b) to write  $q_t = M - G_M \theta_e$ . In addition, from equation (2.17) we deduce

$$(q_t - q_r)H_u = \frac{1}{D_M}(M_r - G_M \theta)H_u. \quad (2.21)$$

Then, as before, using the fact that  $\theta_e$  is given by (2.6a) and  $q_v = (q_t - q_r)H_u + q_{vs}H_s$  is given by (2.4a), we may write

$$q_t = M - G_M \left( \theta + \frac{L_v}{c_p \tilde{\Pi}} \left( \frac{1}{D_M}(M_r - G_M \theta)H_u + q_{vs}H_s \right) \right). \quad (2.22a)$$

This formulation of  $q_t$  in terms of  $\psi$ ,  $M$ , and  $M_r$  may be simplified into the concise form

$$q_t = M + \left( \frac{N_s^2 - N_u^2}{N^2} \right) \left( M_r H_u + \frac{c_p \tilde{\Pi}}{L_v} \theta + q_{vs} H_s \right) \quad (2.22b)$$

by using (2.18). So, the balanced component of the total water mixing ratio is given by the equation (2.22b) above. Notice that this equation depends on the  $M$ ,  $M_r$ , and  $\psi$  variables of the PQG system for prescribed background profiles of  $N_u^2$ ,  $N_s^2$ ,  $\tilde{\Pi}$ , and  $q_{vs}$ .

### 3 Potential Vorticity Inversion

In this section, we discuss different methods that may be used to recover the streamfunction of the balanced system. In principle, this process amounts to the inversion of the QG elliptic operator in (2.14b) using suitable boundary data for a known potential vorticity  $PV_e$  and moisture variable  $M_r$ . In practice, however, different methods may be attempted to approximate the streamfunction.

#### 3.1 Estimate using the pressure

A simple estimate for the streamfunction may be produced as follows. For mid-latitude synoptic atmospheric flows, one natural idea is to consider the pressure—which may be easily obtainable from simulations or atmospheric data—as a proxy for the streamfunction. Namely, for flows in near geostrophic balance, actual pressure is not expected to be significantly different from the balanced pressure arising from the streamfunction. This would entail estimating the requisite streamfunction  $\psi$  by

$$\psi \approx \psi_0 = \frac{p}{f\bar{\rho}}, \quad (3.1)$$

where the subscript 0 is used to connote that this is a “zeroth” order estimate. Therefore, the function  $\psi_0$  is an estimate of  $\psi$  in the sense that it satisfies the equations (2.7a)–(2.7b) of hydrostatic and geostrophic balance approximately.

Although, this method is not, strictly speaking, an inversion procedure, it represents a legitimate avenue for estimation of the streamfunction. The appeal of this method is its relative simplicity and ease of implementation. We include it here mainly for comparison with other more mathematically justifiable methods.

#### 3.2 Inversion of dry QG PV

Another avenue to estimate the streamfunction involves the inversion of equation (2.14b) in a “one phase” case. Specifically, we consider solving the inversion (2.14b) under the assumption that  $H_u = 1$  and  $H_s = 0$  everywhere in the domain, i.e., the domain is strictly unsaturated. As justification for this simplification, we are motivated by the fact that the fraction of the domain that is saturated is expected to be small in mid-latitude atmospheric dynamics. The inversion

equation in this solely unsaturated case then becomes

$$\nabla_H^2 \psi + \frac{1}{\tilde{\rho}} \frac{\partial}{\partial z} \left( \tilde{\rho} \frac{f^2}{N_u^2} \frac{\partial \psi}{\partial z} \right) = PV_e - \frac{1}{\tilde{\rho}} \frac{\partial}{\partial z} \left( \tilde{\rho} \frac{g}{f\theta} \frac{L_v}{c_p \Pi} \frac{f^2}{N_u^2} M_r \right). \quad (3.2)$$

Inversion equation (3.2) gives rise to two immediate observations. First, the inversion still requires for both  $PV_e$  and  $M_r$  to be specified; the potential vorticity  $PV_e$  and moisture variable  $M_r$  are then constructed using the definitions (2.9a) and (2.9b). Second, the absence of the phase indicator functions  $H_u$ ,  $H_s$  means that the buoyancy frequency coefficients  $N^2$  are continuous, though still non-constant.

To carry out the one phase inversion (3.2), suitable boundary information for the streamfunction must be specified. For our purposes we will consider periodicity in the  $x$  direction and Neumann boundary conditions in the  $y$ ,  $z$  directions. Equations (2.7a)–(2.7b) imply that the Neumann conditions require us to specify the potential temperature  $\theta$  at the top and bottom boundaries of our domain and the East-West (zonal) velocity  $u$  in the South and North boundaries of the domain.

We denote the solution of (3.2) by  $\psi_1$ , where the subscript denotes that this is a “one phase” solution.

### 3.3 Inversion of PQG PV

We may also consider the inversion of (2.14b) with two phases of moisture. Namely, we solve

$$\nabla_H^2 \psi + \frac{1}{\tilde{\rho}} \frac{\partial}{\partial z} \left( \tilde{\rho} \frac{f^2}{N^2} \frac{\partial \psi}{\partial z} \right) = PV_e - \frac{1}{\tilde{\rho}} \frac{\partial}{\partial z} \left( \tilde{\rho} \frac{g}{f\theta} \frac{L_v}{c_p \Pi} \frac{f^2}{N^2} (M_r H_u + q_{vs} H_s) \right) \quad (3.3)$$

for the streamfunction  $\psi$  with  $PV_e$  and  $M_r$  specified. As in the one phase case of Section 3.2, we consider a periodic boundary condition in  $x$  and Neumann conditions in  $y$  and  $z$ .

For a completely balanced flow, as arises from QG dynamics, solving (3.3) for the streamfunction could be done with both discontinuous coefficients and nonlinearities arising from the phase indicator functions  $H_u$  and  $H_s$  [43]. Here, instead, as a method for decomposing flows with both balanced and unbalanced components, the phase indicators  $H_u$  and  $H_s$  are influenced by both the balanced and unbalanced components of the system, and they will be treated as given functions, which yields a linear problem (with discontinuous coefficients). That is, we treat the phase interface as known here. For the QG case of the nonlinear inversion problem where the phase interface is unknown, methods are currently under development (C.-N. Tzou and S. N. Stechmann, personal communication).

We label solutions of this inversion procedure by  $\psi_2$ , where the subscript 2 denotes that this is a “two phase” solution of the inversion.

### 3.4 Numerical method

To solve the inversions discussed in Sections 3.2–3.3, we use the following simple numerical method. First, we discretize the differential operator using centered differences on a staggered grid (e.g., [22]). This step would be standard and second-order accurate if the coefficients of the PDE were smooth, but it is slightly complicated due to the discontinuity of the buoyancy frequency coefficients. As a result, the method is only first-order accurate, and it is similar to the ghost fluid method [27, 28]. Rather than using the more complex version with sub-cell interface locations [27], our implementation uses the simpler setup with all functions evaluated at their respective grid points, similar to [28]. Second, the discretized system is then inverted using the conjugate gradient method for symmetric matrices (e.g., [46]).

The discretization of the system is done on the interior points of the grid which range over the indices  $i \in [1, I]$ ,  $j \in [1, J]$ ,  $k \in [1, K]$ . Thus, grid cell “edges” are located halfway between interior points, e.g.,  $(i - \frac{1}{2}, j, k)$  and  $(i + \frac{1}{2}, j, k)$  are edges for the point  $(i, j, k)$ . The boundaries of the domain are then at the points  $i = \frac{1}{2}, I + \frac{1}{2}$ ,  $j = \frac{1}{2}, J + \frac{1}{2}$ , and  $k = \frac{1}{2}, K + \frac{1}{2}$ . The discretization of the differential operator then follows the standard form at the grid point  $(i, j, k)$ :

$$\tilde{\rho}_k \nabla_H^2 \psi_{i,j,k} + \tilde{\rho}_{k+\frac{1}{2}} \frac{f^2}{N_{k+\frac{1}{2}}^2} \left( \frac{\psi_{i,j,k+1} - \psi_{i,j,k}}{(\Delta z)^2} \right) - \tilde{\rho}_{k-\frac{1}{2}} \frac{f^2}{N_{k-\frac{1}{2}}^2} \left( \frac{\psi_{i,j,k} - \psi_{i,j,k-1}}{(\Delta z)^2} \right) = F_{i,j,k}, \quad (3.4a)$$

where  $\nabla_H^2 \psi_{i,j,k}$  is the usual discrete Laplacian

$$\nabla_H^2 \psi_{i,j,k} = \frac{\psi_{i+1,j,k} - 2\psi_{i,j,k} + \psi_{i-1,j,k}}{(\Delta x)^2} + \frac{\psi_{i,j+1,k} - 2\psi_{i,j,k} + \psi_{i,j-1,k}}{(\Delta y)^2} \quad (3.4b)$$

and

$$F(x, y, z) = \tilde{\rho} P V_e - \frac{\partial G}{\partial z} \quad \text{with} \quad G(x, y, z) = \tilde{\rho} \frac{g}{f\tilde{\theta}} \frac{L_v}{c_p \tilde{\Pi}} \frac{f^2}{N^2} (M_r H_u + q_{vs} H_s) \quad (3.4c)$$

which is discretized as

$$F_{i,j,k} = \tilde{\rho}_k (P V_e)_{i,j,k} - \left( \frac{G_{i,j,k+\frac{1}{2}} - G_{i,j,k-\frac{1}{2}}}{\Delta z} \right). \quad (3.4d)$$

The streamfunction  $\psi_{i,j,k}$  for the indices  $i = 0, I + 1$ ,  $j = 0, J + 1$ , and  $k = 0, K + 1$  lies outside the grid and must be specified in some form. At the  $i = \frac{1}{2}, I + \frac{1}{2}$  boundaries of the domain, we assume periodicity, i.e.,

$$\psi_{0,j,k} = \psi_{I,j,k} \quad \text{and} \quad \psi_{1,j,k} = \psi_{I+1,j,k}. \quad (3.4e)$$

For the  $y$  and  $z$  boundaries we use discretizations of the conditions (2.7a)–(2.7b) as our Neumann conditions. Namely, we set

$$-u_{i,\frac{1}{2},k} = \frac{\psi_{i,1,k} - \psi_{i,0,k}}{\Delta y} \quad \text{and} \quad -u_{i,J+\frac{1}{2},k} = \frac{\psi_{i,J+1,k} - \psi_{i,J,k}}{\Delta y}, \quad (3.4f)$$

$$g \frac{\theta_{i,j,\frac{1}{2}}}{\tilde{\theta}_{\frac{1}{2}}} = f \frac{\psi_{i,j,1} - \psi_{i,j,0}}{\Delta z} \quad \text{and} \quad g \frac{\theta_{i,j,K+\frac{1}{2}}}{\tilde{\theta}_{K+\frac{1}{2}}} = f \frac{\psi_{i,j,K+1} - \psi_{i,j,K}}{\Delta z} \quad (3.4g)$$

where  $u$  and  $\theta$  are specified functions at the given boundary.

Finally, note that one could possibly use a second-order accurate numerical method [9, 24, 25, 23, 47] instead of a first-order accurate method, but a first-order accurate method is simpler and is sufficient for the purposes of the present paper.

## 4 Streamfunction Inversion in a Simplified Setting

In this section, we describe the difference between the streamfunctions and temperatures obtained from the one phase inversion discussed in Section 3.2 and the two phase inversion of Section 3.3 in a simplified setting. Namely, we use simplified anelastic background states and simplified anomaly variables to observe the difference our choice of inversion and anomaly variables has on the resultant streamfunction. Both the background states and anomaly variables of this section are physically motivated, but are primarily chosen for their analytical simplicity. We observe that the moisture choice, in particular, the choice of cloud water  $q_c$ , can have a significant impact on the structure of the streamfunction and temperature. In other words, all else held equal, the location of the transition between phases, the choice of background states in saturated regions, and the quantity of cloud water in saturated regions affect the streamfunction.

### 4.1 Anelastic background state

We begin by describing the simplified anelastic background state we will use to study the effects of moisture on the streamfunction obtained from one and two phase inversions. Our goal in choosing our background states is for them to be both physically sensible and analytically tractable. First, we require the background states to satisfy the equations

$$\frac{d\tilde{p}}{dz} = -\tilde{\rho}g, \quad (4.1a)$$

$$\tilde{p} = \tilde{\rho}R_d\tilde{T}, \quad (4.1b)$$

$$\tilde{\theta} = \tilde{T}\left(\frac{p_0}{\tilde{p}}\right)^{R_d/c_p}, \quad (4.1c)$$

where equation (4.1a) corresponds to hydrostatic balance, (4.1b) is the ideal gas law, and (4.1c) is the definition of potential temperature. Note that equations (4.1a)–(4.1c) entail that only one of  $\tilde{\rho}$ ,  $\tilde{p}$ ,  $\tilde{T}$ , or  $\tilde{\theta}$  may be chosen freely, with all others then determined. For simplicity we choose the following background potential temperature:

$$\tilde{\theta} = \theta_0 + Bz, \quad (4.2a)$$

where  $\theta_0 = 280$  K and  $B = 5$  K/km are chosen to roughly match a low altitude mid-latitude profile [35, Fig. 5.8]. A comprehensive list of relevant parameters and their mid-latitude values

is given in Table 1. For this potential temperature profile, equations (4.1a)–(4.1c) determine the background state pressure

$$\tilde{p} = p_0 \left( 1 - \frac{g}{Bc_p} \log \left( 1 + \frac{Bz}{\theta_0} \right) \right)^{c_p/R_d}, \quad (4.2b)$$

where  $p_0 = 10^5$  Pa is the value of the pressure at the surface; we refer the interested reader to [12] for a careful derivation of the pressure (4.2b) from profile (4.2a) and equations (4.1a)–(4.1c). From the background potential temperature (4.2a) and pressure (4.2b), the background temperature  $\tilde{T}$  can then be found by means of (4.1c) and the background density  $\tilde{\rho}$  may be found by means of (4.1b).

Note that equations (4.1a)–(4.1c) do not specify the background moisture. So, we freely choose the background water vapor to be

$$\tilde{q}_v = q_{v,0} \exp(-Cz), \quad (4.2c)$$

where  $q_{v,0} = 8$  g/kg and  $C = 1/5$  km<sup>−1</sup> are again chosen to be physically sensible for mid-latitudes [35, Fig. 5.15]. The form of the background state density  $\tilde{\rho}$ , pressure  $\tilde{p}$ , potential temperature  $\tilde{\theta}$ , and water vapor  $\tilde{q}_v$  is shown in Figure 1.

Additionally, the water vapor saturation profile may be determined in approximate form using the Clausius-Clapeyron relation [12, 40]. Namely, we define the total saturation profile to be  $q_{vs}^{\text{tot}}(z) = q_{vs}(\tilde{p}(z), \tilde{T}(z)) \approx q_{vs}(p, T)$ , where the saturation profile  $q_{vs}(p, T)$  is obtained from the total pressure and the Clausius-Clapeyron formula for saturation vapor pressure dependent on the temperature  $T$ . This gives the equation

$$q_{vs}^{\text{tot}} = \frac{q_{vs,0}}{\tilde{p}/p_0} \exp \left( -\frac{L_v}{R_v} \left( \frac{1}{\tilde{T}} - \frac{1}{\theta_0} \right) \right), \quad (4.3a)$$

where  $q_{vs,0} = 20$  g/kg is the surface water vapor saturation value. Then, the saturation water vapor (anomaly) that will be used to determine the phase transitions, e.g., using relations (2.3a)–(2.3b), is then

$$q_{vs} = q_{vs}^{\text{tot}} - \tilde{q}_v. \quad (4.3b)$$

Lastly, the background potential temperature  $\tilde{\theta}$  (4.2a) and water vapor  $\tilde{q}_v$  (4.2c) with equation (2.6a) for  $\tilde{\theta}_e$  allow us to determine the buoyancy frequencies  $N_u^2(z)$  and  $N_s^2(z)$  defined by equations (2.13). The form of the buoyancy frequencies is shown in Figure 2.

## 4.2 Simplified anomaly variables

In this section, we describe the simplified anomaly variables that we will use in each of our streamfunction inversions. The choice of these variables will determine not only what may be acceptable boundary conditions for the inversion procedure, but also the location of phase transitions. In principle, each streamfunction inversion requires us to specify both the equivalent potential vorticity  $PV_e$  and moisture variable  $M_r$ . It is perhaps easier, however, to

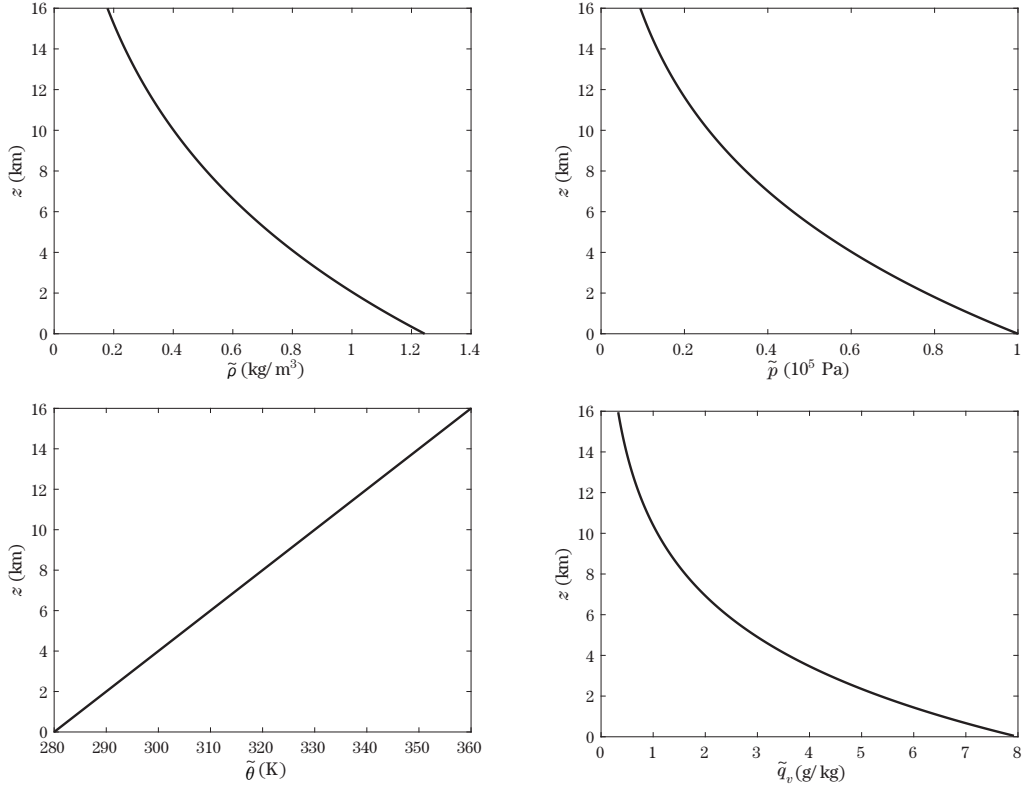


Figure 1 Anelastic background states satisfying equations (4.1a)–(4.1c), (4.2a), and (4.2c). Top left: background density  $\tilde{\rho}$ . Top Right: background pressure  $\tilde{p}$ . Bottom left: background potential temperature  $\tilde{\theta}$ . Bottom right: background water vapor  $\tilde{q}_v$ .

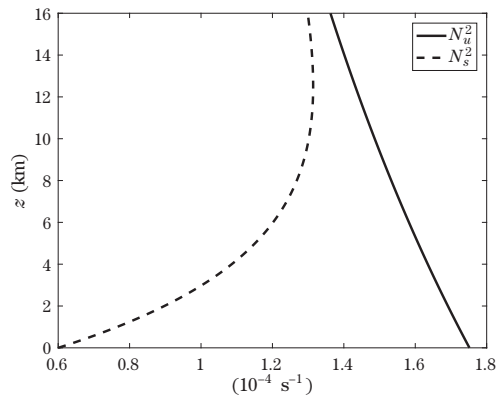


Figure 2 Buoyancy frequencies for unsaturated regions  $N_u^2$  (solid line) and saturated regions  $N_s^2$  (dashed line).

construct these variables from simpler variables related to the moisture and streamfunction. In this case, we choose to use the moisture  $q_t - q_r$  and a streamfunction like function  $\varphi$ . The

Table 1 List of parameters used in this paper with typical (northern hemisphere) mid-latitude values.

Parameter	Typical Value	Definition
$f$	$10^{-4} \text{ s}^{-1}$	Coriolis parameter
$g$	$9.81 \text{ m/s}^2$	Acceleration due to gravity
$L_v$	$2.5 \times 10^6 \text{ J kg}^{-1}$	Latent heat factor
$c_p$	$10^3 \text{ J kg}^{-1} \text{ K}^{-1}$	Specific heat at constant pressure
$R_d$	$287 \text{ J kg}^{-1} \text{ K}^{-1}$	Dry air gas constant
$R_v$	$462 \text{ J kg}^{-1} \text{ K}^{-1}$	Water vapor gas constant
$p_0$	$10^5 \text{ Pa}$	Reference surface pressure
$\theta_0$	$280 \text{ K}$	Reference surface temperature
$B$	$5 \text{ K km}^{-1}$	Vertical gradient of background temperature
$q_{v,0}$	$8 \text{ g kg}^{-1}$	Reference surface water vapor
$C$	$1/5 \text{ km}^{-1}$	Background water vapor rate of decrease
$q_{vs,0}$	$20 \text{ g kg}^{-1}$	Reference surface saturation water vapor
$A_0$	$10 \text{ g kg}^{-1}$	Surface value of moisture anomaly
$A_1$	$-1 \text{ g kg}^{-1} \text{ km}^{-1}$	Vertical gradient of moisture anomaly
$L$	$1,000 \text{ km}$	Horizontal reference scale for QG dynamics
$H$	$10 \text{ km}$	Vertical reference scale for QG dynamics
$U$	$10 \text{ m/s}$	Velocity reference scale for QG dynamics

potential vorticity  $PV_e$  and moisture variable  $M_r$  will then be defined by

$$PV_e = \nabla_H^2 \varphi + \frac{f}{\tilde{\rho}} \frac{\partial}{\partial z} \left( \frac{\tilde{\rho}}{d\tilde{\theta}_e/dz} \left( \frac{f\tilde{\theta}}{g} \frac{\partial \varphi}{\partial z} + \frac{L_v}{c_p \tilde{\Pi}} ((q_t - q_r)H_u + q_{vs}H_s) \right) \right), \quad (4.4a)$$

$$M_r = q_t - q_r + G_M \left( \frac{f\tilde{\theta}}{g} \frac{\partial \varphi}{\partial z} + \frac{L_v}{c_p \tilde{\Pi}} ((q_t - q_r)H_u + q_{vs}H_s) \right) \quad (4.4b)$$

for prescribed variables  $q_t - q_r$  and  $\varphi$ . As before, the indicator functions  $H_u$  and  $H_s$  are determined to be consistent with the phase conditions (2.11) for the chosen  $q_t - q_r$  and  $q_{vs}$ . Thus, once  $q_t - q_r$  and  $\varphi$  are chosen,  $PV_e$  and  $M_r$  are determined and are kept the same for both inversion cases.

We will consider two different formulations for the  $q_t - q_r$  and  $\varphi$  variables. One formulation will be chosen so that  $q_t - q_r$  and  $\varphi$  are uniform in the horizontal directions (uniform in  $x$  and  $y$ ), while the other formulation will have  $x$  and  $y$  variation. Namely, for simplicity we choose the moisture variable  $q_t - q_r$  to satisfy either

$$q_t - q_r = A_0 + A_1 z \quad (4.5a)$$

or

$$q_t - q_r = \frac{1}{3}(A_0 + zA_1) \left( 2 - \cos\left(\frac{4\pi}{L_x}x\right) \cos\left(\frac{2\pi}{L_y}y\right) \right). \quad (4.5b)$$

Here, we choose the parameters  $A_0 = 10 \text{ g/kg}$  and  $A_1 = -1 \text{ (g/kg) km}^{-1}$  related to the moisture profile and  $L_x = 12,000 \text{ km}$  and  $L_y = 8,000 \text{ km}$  related to the domain geometry. We show the

moisture variable  $q_t - q_r$  for both (4.5a) and (4.5b) for the saturation water vapor (4.3a)–(4.3b) in Figure 3. Notice that the region where  $q_t - q_r > q_{vs}$  corresponds to a saturated region; for our chosen moisture profiles saturation occurs approximately between  $2 \text{ km} \leq z \leq 10 \text{ km}$ . Since  $q_c = q_t - q_r - q_{vs}$  by definition (2.4b), the excess of  $q_t - q_r$  above the saturation water vapor  $q_{vs}$  corresponds to cloud water and can be seen to have a maximum of about  $2.5 \text{ g/kg}$  at  $z = 6 \text{ km}$  for (4.5a) and two maxima of about  $2.5 \text{ g/kg}$  at  $(x, y, z) = (3000, 4000, 6) \text{ km}$  and  $(x, y, z) = (9000, 4000, 6) \text{ km}$  for (4.5b). Lastly, we note that the values of  $q_t - q_r$  at high altitudes are not wholly realistic as they would require a very large and negative rainwater  $q_r$  profile to be true, but we neglect this fact in favor of the relative simplicity of the moisture profile.

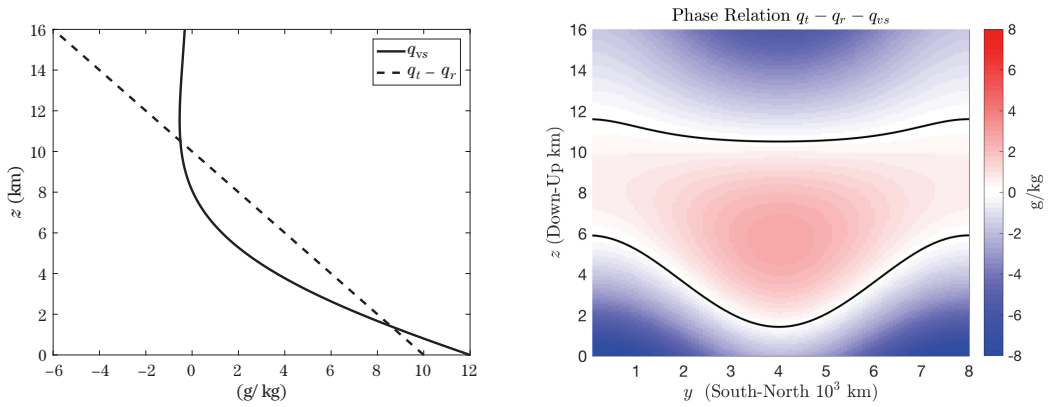


Figure 3 Saturation water vapor  $q_{vs}$  from (4.3a)–(4.3b) with moisture anomaly  $q_t - q_r$ . Left:  $q_{vs}$  (solid line) and  $q_t - q_r$  (dashed line) given by (4.5a) in the simplified setting. Right:  $q_t - q_r - q_{vs}$  for  $q_t - q_r$  given by (4.5b); solid black lines represent phase relation  $q_t - q_r - q_{vs}$ .

Next, we similarly consider two formulations of for the variable  $\varphi$ . In particular, we consider either

$$\varphi = UL \cos\left(\frac{6\pi}{L_z}z\right) \quad (4.6a)$$

or

$$\varphi = UL \cos\left(\frac{4\pi}{L_x}x\right) \cos\left(\frac{2\pi}{L_y}y\right) \cos\left(\frac{6\pi}{L_z}z\right). \quad (4.6b)$$

Here, we choose  $U = 10 \text{ m/s}$  and  $L = 10^6 \text{ m}$  as realistic mid-latitude geostrophic values [48] and  $L_z = 16 \text{ km}$  as the height of the domain.

Therefore, we construct the potential vorticity  $PV_e$  and moisture variable  $M_r$  via (4.4a)–(4.4b) by using (1) the formulation (4.5a) and (4.6a) to obtain a uniform in  $x$  and  $y$  system and (2) the formulation (4.5b) and (4.6b) which gives a system with variability in  $(x, y, z)$ . We show the potential vorticity  $PV_e$  and moisture variable  $M_r$  using (4.5a) and (4.6a) in Figure 4 and those obtained using (4.5b) and (4.6b) in Figure 5.

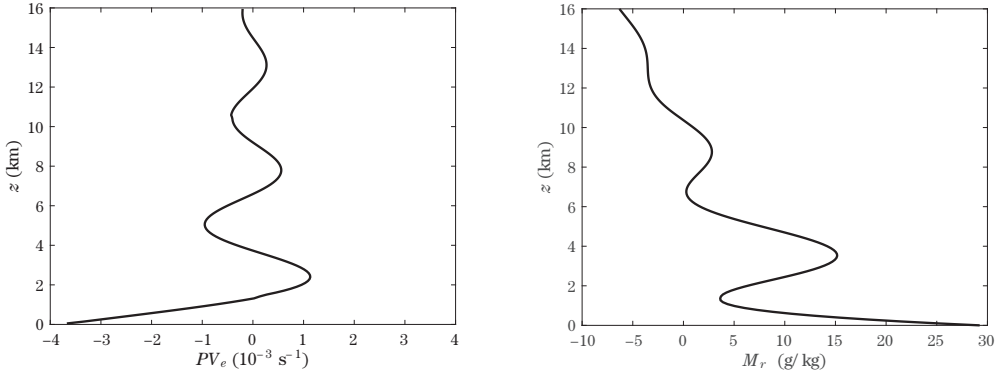


Figure 4 Left: Equivalent potential vorticity  $PV_e$  for the uniform in  $x$  and  $y$  formulation (4.5a) and (4.6a). Right: Moisture variable  $M_r$  for the same formulation.

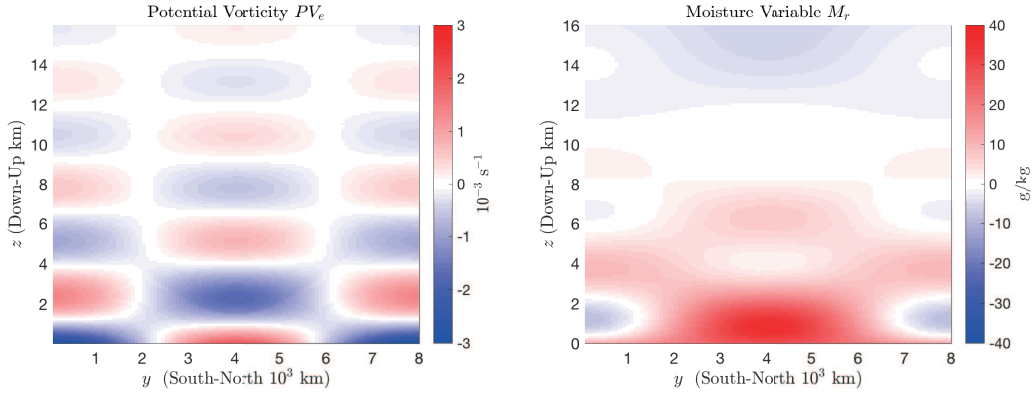


Figure 5 Left: Equivalent potential vorticity  $PV_e$  for the fully three-dimensional (4.5b) and (4.6b) formulation. Right: Moisture variable  $M_r$  for the same formulation.

### 4.3 Comparison of one and two phase inversions

Using the anomaly variables  $PV_e$  and  $M_r$  of Section 4.2 with the background state of Section 4.1, we may recover the streamfunction by inverting (2.14b) using the numerical method specified in Section 3.4. We are then additionally able to compute the balanced potential temperature arising from the streamfunction by means of equations (2.7a) and (2.7d). We do the streamfunction inversion in two ways: first, we consider the one phase inversion outlined in Section 3.2 and, second, we consider the two phase inversion described in Section 3.3. For each inversion we impose the following boundary conditions: periodicity in the  $x$  direction,  $\frac{\partial \psi}{\partial y} = 0$  on  $y = 0, L_y$ , and  $\frac{\partial \psi}{\partial z} = 0$  on  $z = 0, L_z$ . In addition, to understand the effect that our choice of anomalies has on the streamfunction we use both the uniform in  $y, z$  formulation (4.5a) and (4.6a) and the fully three-dimensional formulation (4.5b) and (4.6b).

The streamfunction and balanced potential temperature from the one phase (denoted with a subscript 1) and two phase (denoted with a subscript 2) inversions using  $PV_e$  and  $M_r$  for

the uniform in  $x$  and  $y$  formulation are shown in Figure 6. Notice that the balanced one and two phase streamfunctions and temperatures differ significantly in the location of the region of saturation; in this case, saturation occurs between  $2 \leq z \leq 10$  km as shown in left plot of Figure 3. In particular, an excess of cloud water of about  $q_c \approx 3$  g/kg (left plot in Figure 3) leads to a difference of about 8 K in the temperature (bottom plots in Figure 6) or about a 20% change in the amplitude. The one phase temperature appears to be strictly lower than the two phase temperature. Moreover, the length scale of the difference between one and two phase solutions is comparable to the length scale of cloud water  $q_c$  features.

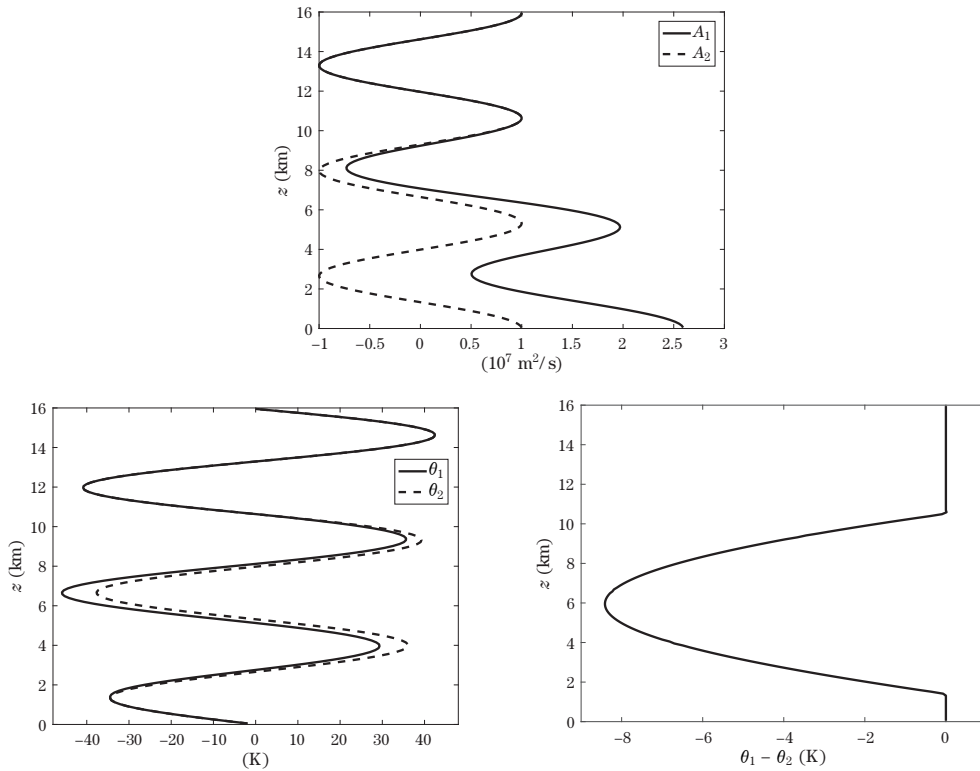


Figure 6 Streamfunction  $\psi$  (top) and potential temperature  $\theta$  (bottom) arising from inversion using  $PV_e$  and  $M_r$  given by uniform (4.5a) and (4.6a). Subscript 1 refers to one phase inversion while subscript 2 refers to two phase inversion.

Similarly, the potential temperature and the difference between the potential temperature from the one and two phase inversions is shown in Figure 7 for the fully three-dimensional  $PV_e$  and  $M_r$  of (4.5b) and (4.6b). As in the 1D case, we observe that an excess of  $q_c \approx 3$  g/kg (right on Figure 3) in cloud water leads to a 7 K difference in temperature. Moreover, we find that the region where the significant difference between the two temperature fields occurs is strongly linked to the location where the system is saturated; compare the region of saturation of the right plot in Figure 3 with the region in Figure 7. As before, the difference is such that the

temperature of the one phase inversion is lower than that of the two phase case. This, however, is no longer strictly true everywhere in the domain; observe that the two phase temperature is higher at  $(y, z) = (4000, 12)$  km, which is inside the unsaturated region of the domain.

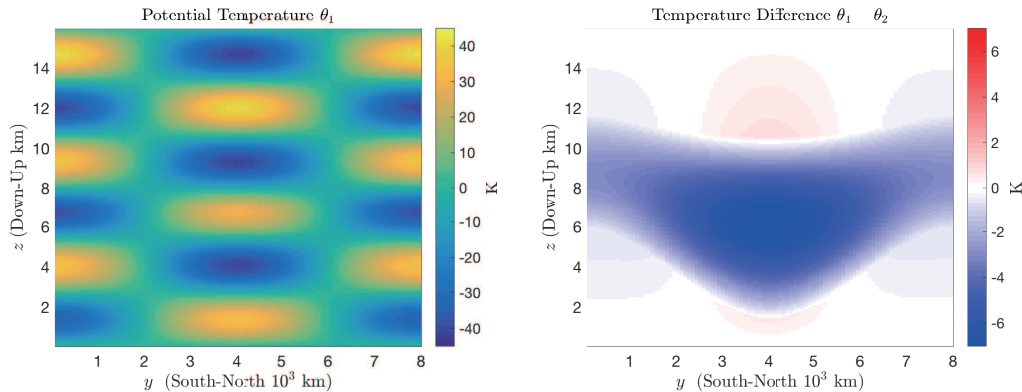


Figure 7 Potential temperature  $\theta_1$  obtained from one phase inversion (left) and difference between temperatures in one and two phase inversions (right). Both streamfunction inversions performed using  $PV_e$  and  $M_r$  given by (4.5b) and (4.6b).

It is perhaps not surprising that the differences between the solutions of the two inversion procedures are strongest in the locations where the system is saturated; the key difference between the one and two phase inversions is the incorporation of saturated regions into the inversion. We may indeed clarify this point slightly by considering the difference between the two inversion procedures.

#### 4.4 Difference between one and two phase inversions

We note briefly that by taking the difference (3.2) and (3.3) it is possible to write down a simple PDE satisfied by the difference between the streamfunctions, i.e.,  $\psi_2 - \psi_1$ . Specifically, the difference between the solutions of the one and two phase inversions can be written as

$$\nabla_H^2(\psi_2 - \psi_1) + \frac{1}{\tilde{\rho}} \frac{\partial}{\partial z} \left( \tilde{\rho} \frac{f^2}{N^2} \frac{\partial}{\partial z} (\psi_2 - \psi_1) \right) = \frac{1}{\tilde{\rho}} \frac{\partial}{\partial z} \left( \tilde{\rho} \frac{g}{f\theta} \frac{L_v}{c_p \Pi} \frac{f^2}{N_u^2} q_c \right) \quad (4.7)$$

simplifying by means of equation (2.6a) for  $\theta_e$ , equation (2.9c)  $M_r$ , and equation (2.18) and the fact that both inversions require the same  $PV_e$  and  $M_r$  variables. Therefore, the difference between the two inversion procedures is related to the cloud water and the location of phase transitions.

## 5 Simulated Data

Here, we use data from an equilibrated turbulent synoptic mid-latitude numerical simulation to determine balanced components for the temperature and velocity by means of the procedures of Section 3. Notice that data arising from a large scale mid-latitude simulation

fits naturally within the QG inversion or approximate QG balance framework of Section 3. We proceed analogously to Section 4 by constructing potential vorticity  $PV_e$  and moisture variable  $M_r$  to recover the streamfunction. The balanced variables that arise from these different streamfunction are then compared and the effects of the different inversions on the solutions are discussed. We begin by describing the numerical model chosen and the simulation setup.

### 5.1 Description of WRF numerical code and setup

For our numerical simulations we use version 3.7.1 of the Weather Research and Forecast (WRF; [42]) model developed by the National Center for Atmospheric Research (NCAR). The WRF model solves the compressible, non-hydrostatic Euler equations using a terrain-following hydrostatic-pressure vertical coordinate with C-grid staggering and a time-split integration scheme. Our simulation consists of a generalization of the idealized default unstable baroclinic wave case `em_b_wave` available within the WRF package. Namely, we configure the model to run a  $\beta$ -plane mid-latitude channel simulation. The physics parameterization used for this simulation is that of the Kessler microphysics scheme [15], which contains warm moisture constituents of rainwater, cloud water, and water vapor. We include no short- or long-wave radiation, no surface or boundary layer physics, and no cumulus physics schemes.

The channel geometry is chosen to be  $L_x \times L_y \times L_z = 12,000 \text{ km} \times 8,000 \text{ km} \times 16 \text{ km}$  in the West-East, South-North, and Down-Up directions, respectively. The resolution of the simulation is selected to be  $\Delta x = \Delta y = 25 \text{ km}$ , giving 480 equally spaced grid points in the East-West and 320 points in the South-North direction, and 64 grid points in the vertical direction, accounting for an approximate  $\Delta z \approx 250 \text{ m}$  resolution in the vertical. The time-step chosen is  $\Delta t = 40$  seconds. The  $\beta$ -plane is chosen with the following parameters:  $f_0 = 10^{-4} \text{ s}^{-1}$  at the center of the channel and  $\beta = 10^{-8} \text{ s}^{-1} \text{ km}^{-1}$  as the south-north gradient, i.e.,  $f = f_0 + \beta(y - y_0)$ , where  $f$  is the Coriolis frequency and  $y_0 = L_y/2 = 4,000 \text{ km}$  is the reference position at the center of the channel.

Lastly, we impose periodic boundary conditions in the  $x$  (East-West) direction and specify the boundary values in the South and North walls of the channel. At these specified boundaries we use a relaxation zone of 4 grid points. Therefore, the south and north boundary conditions are rigid and specified. The specific boundary values used at the south and north walls of the channel are discussed in more detail in the next section.

### 5.2 Background state and boundary conditions

The background state and boundary conditions for the numerical simulation are chosen to be physically relevant for a mid-latitude flow. These values themselves are taken from the default WRF package `em_b_wave`. We show the anelastic background state used in the numerical simulation in Figure 8. Similarly, the uniform in  $x$  (East-West) south and north boundary values are shown in Figure 9. For the boundary data, we note that the water vapor chosen has a significant signal at the southern boundary. Namely, the southern boundary will

maintain a high level of water vapor that will then flow into the channel through this wall. In this way, the total moisture in the channel is controlled by these chosen boundaries values.

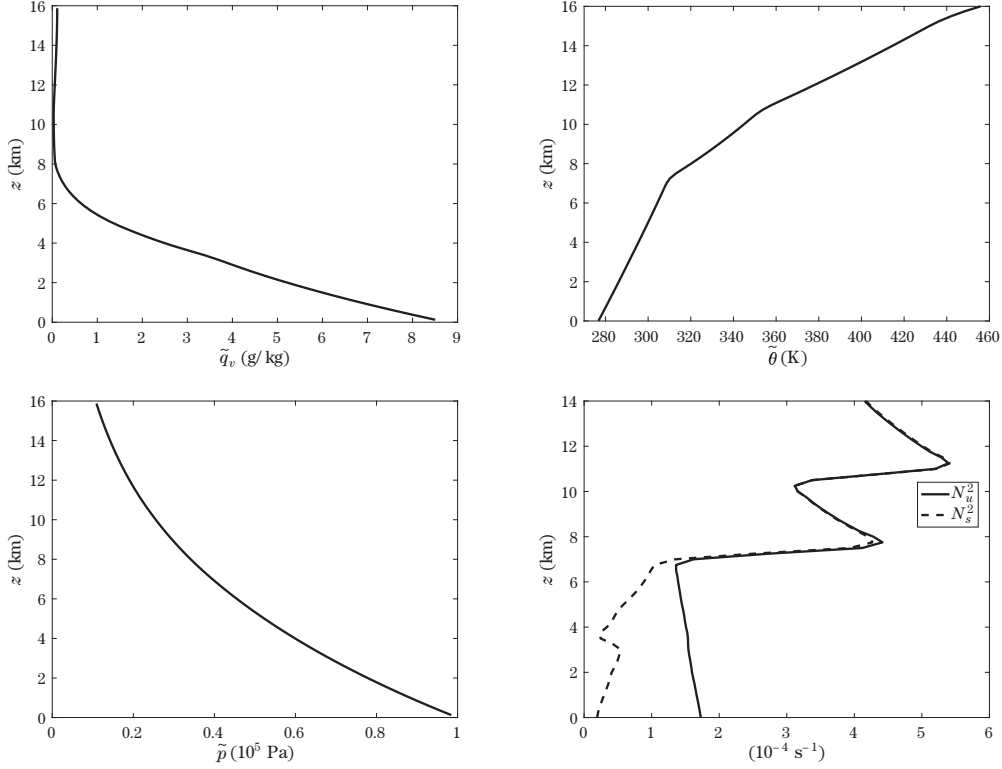


Figure 8 Anelastic background states used in the WRF numerical simulation.

### 5.3 Snapshots of simulated data

We run the numerical simulation of the WRF model beginning from an unstable baroclinic wave initial condition. We do not describe this initial condition in detail since it is that found in the default `em_b_wave` case and our interest lies in the equilibrated state. In this simulation, nonlinear effects become significant at around 8 days and equilibration of the solution is achieved after about 40 days of simulation time. For the remainder of this section, we consider the simulation data at 100 days since the system is well equilibrated and turbulence is sufficiently developed at that time.

To give a sense of the simulated data at 100 days, we show a series of cross-sections at 4 km height of the turbulent channel flow and a 3D visualization of the cloud water in Figure 10. At 100 days we find a significant amount of transport of moisture northward at  $x = 8,000$  km; see  $q_v$  plot in Figure 10. This moisture transport is connected to a broad northward meander of the West-East jet at this height most easily seen in the top picture of Figure 11 for the pressure. In addition, we observe a significant amount of cloud cover in the northern part of the channel

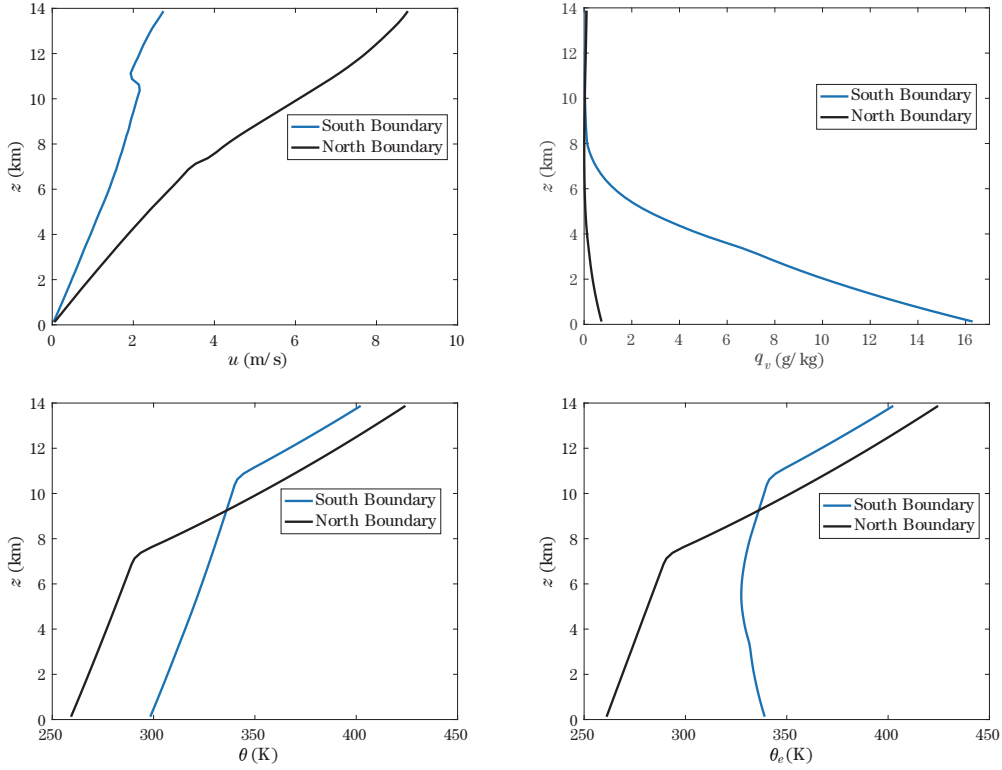


Figure 9 Southern and northern boundary values of velocity  $u$  (top left), water vapor  $q_v$  (top right), potential temperature  $\theta$  (bottom left), and equivalent potential temperature  $\theta_e$  (bottom right) used in WRF simulations.

and broad cloud cover in the region between 5 km and 10 km in height; see  $q_c$  plot and the 3D cloud isosurface plot in Figure 10 .

#### 5.4 Balanced components of simulated data

Since our simulation consists of an equilibrated mid-latitude channel flow, the QG inversions of Section 3 used to construct the balanced flow are directly applicable. For the simulation we compute the balanced components of the velocity and temperature analogously to the simplified case of Section 4. Namely, we construct  $PV_e$  and  $M_r$  variables using the simulated data and use these to recover the balanced streamfunction by means of an inversion process. Unlike the process of Section 4, however, we are also able to compute a streamfunction arising from the pressure as discussed in Section 3.1. The balanced velocity and temperature are then obtained from the respective streamfunction by means of equations (2.7a)–(2.7d). For the inversions we use boundary conditions arising from the simulated data: periodicity in the  $x$  direction,  $\partial\psi/\partial y = -u$  on  $y = 0, L_y$ , and  $\partial\psi/\partial z = g\theta/(f\tilde{\theta})$  on  $z = 0, L_z$ . Here, boundary values of the velocity  $u$  and the temperature  $\theta$  are given by the simulation.

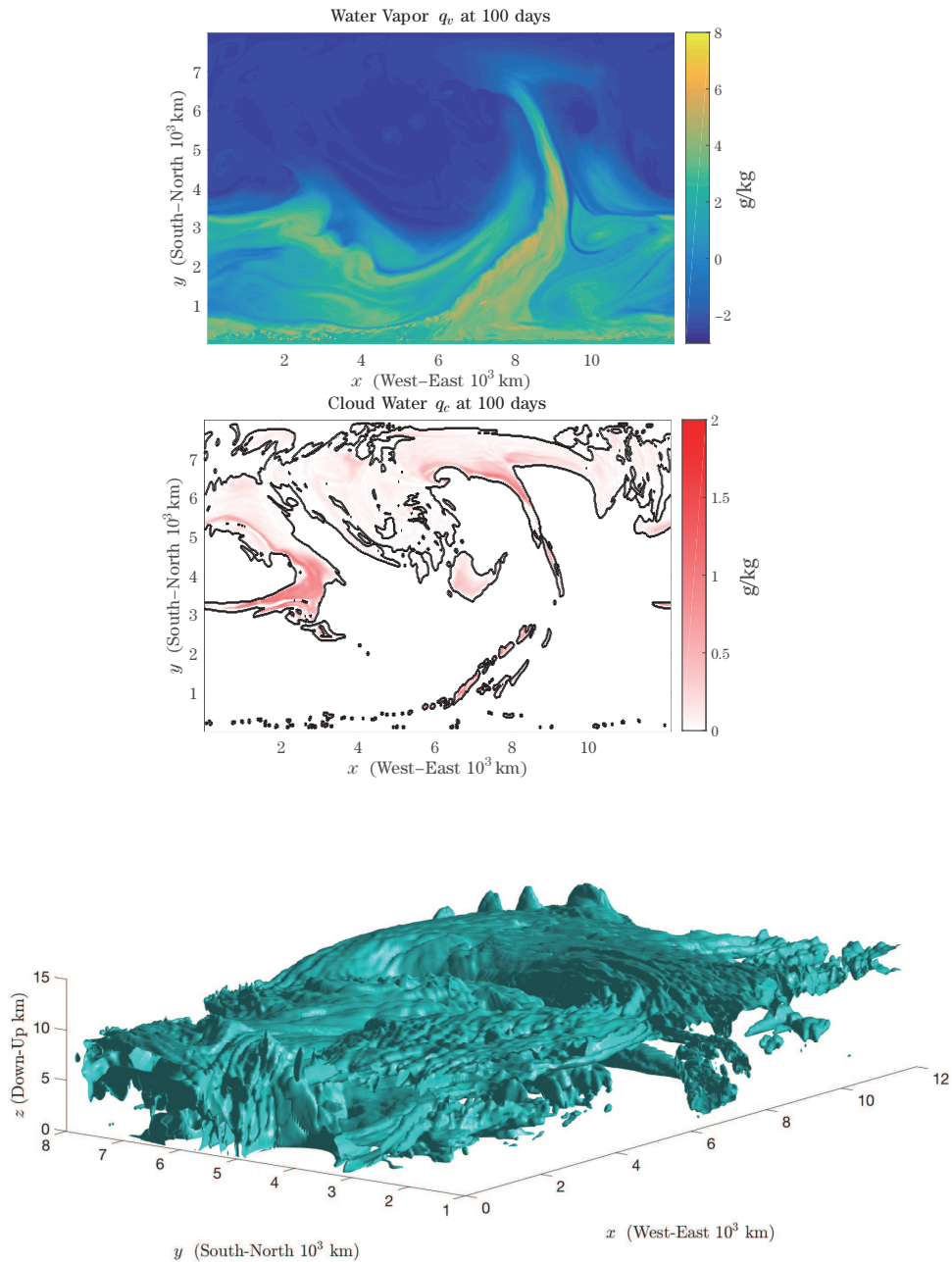


Figure 10 Simulated data at 4 km height 100 days after start of simulation. Top: Water vapor  $q_v$ . Middle: Cloud water  $q_c$  with solid black line for the cloud boundary. Bottom: Cloud water  $q_c$  isosurface  $q_c = 0.01$  g/kg.

We show a cross-section at 4 km height for the streamfunctions obtained from the estimate from pressure and inversion procedures in Figure 11. We note that all streamfunctions produce broadly the same essential features with the streamfunction from pressure broadly agreeing with those obtained from inversion. Namely, all streamfunctions reproduce the large meander

of the flow at  $x \approx 8,000$  km and the two large vortices at  $y \approx 5,000$  km. The West-East jet meander coincides with the northward moisture transport seen in the bottom row of Figure 10. The two vortices, moreover, correspond to areas with significant cloud water coverage.

In terms of the individual streamfunctions, we note that the streamfunction estimated from pressure appears to overestimate the pressure gradient associated with the two northern vortices in comparison to the one and two phase solutions. Similarly, the one and two phase streamfunctions consider the West-East jet to be slightly stronger, with a higher gradient of streamfunction seen in the meander. Differences between the one and two phase streamfunctions appear to be small and localized owing largely to the small cloud water amounts in the saturated regions of the simulation; see bottom plot in Figure 11. Nonetheless, differences between the one and two phase streamfunctions become appreciable on derivatives of the streamfunction: the balanced velocity and temperature.

We may quantify some the differences between the streamfunction estimates by considering the  $L_2$  norm of the data. Namely, below 8 km in height we find that  $\|\psi_1 - \psi_0\|_2 / \|\psi_0\|_2 \approx 0.3062$  and  $\|\psi_2 - \psi_1\|_2 / \|\psi_1\|_2 \approx 0.0106$ , where the subscript 0 denotes the estimate from pressure, the subscript 1 denotes the one phase inversion, and 2 denotes the two phase inversion. That is, the difference between the streamfunction from pressure  $\psi_0$  and the one phase streamfunction  $\psi_1$  below 8 km is roughly 30%, while the difference between the one and two phase streamfunctions below 8 km is about 1%. This is broadly consistent with what is observed on the figures, but we note that these norms may not capture significant small scale variations between the variables.

In addition, we show the cross-sections of the velocity at a 4 km height in Figure 12 and velocity differences, the unbalanced velocities, in Figure 13. These pictures show that large scale features of the velocity are broadly captured by all balanced velocities. Most small scale features of the raw velocity, however, are filtered out below the  $\approx 500$  km level in both the one and two phase balanced velocity. In contrast, the balanced velocity arising from pressure appears to overestimate the amplitudes of large features and significantly overestimates the small scale velocity signature.

As before, we may quantify the bulk differences between the balanced velocities and the raw velocity by considering the  $L_2$  norm of the data. Namely, considering the values of the velocities below 8 km in height we find:  $\|u - u_0\|_2 / \|u\|_2 \approx 0.4664$ ,  $\|u - u_1\|_2 / \|u\|_2 \approx 0.1205$ , and  $\|u_2 - u_1\|_2 / \|u_1\|_2 \approx 0.0180$ . Therefore, the balanced velocity estimated from pressure gives a significantly different velocity signal as those predicted from the one and two phase inversions. The one and two phase inversions are close to each other in the large scale, however, they differ at small scales in regions of saturation. To see this last fact about the one and two phase balanced velocities, we consider the magnitude of the Fourier transform in the  $x$  direction for a fixed  $(y, z)$  of the data and average for all  $y$  values, i.e., the meridional mean of the magnitude of the zonal Fourier transform. Again, we pick the height of  $z = 4$  km and show these results on the left plot of Figure 16. Figure 16 shows that the one and two phase balanced velocities capture the raw velocity at large scales, but begin to differ from it at scales below  $\approx 1000$  km.

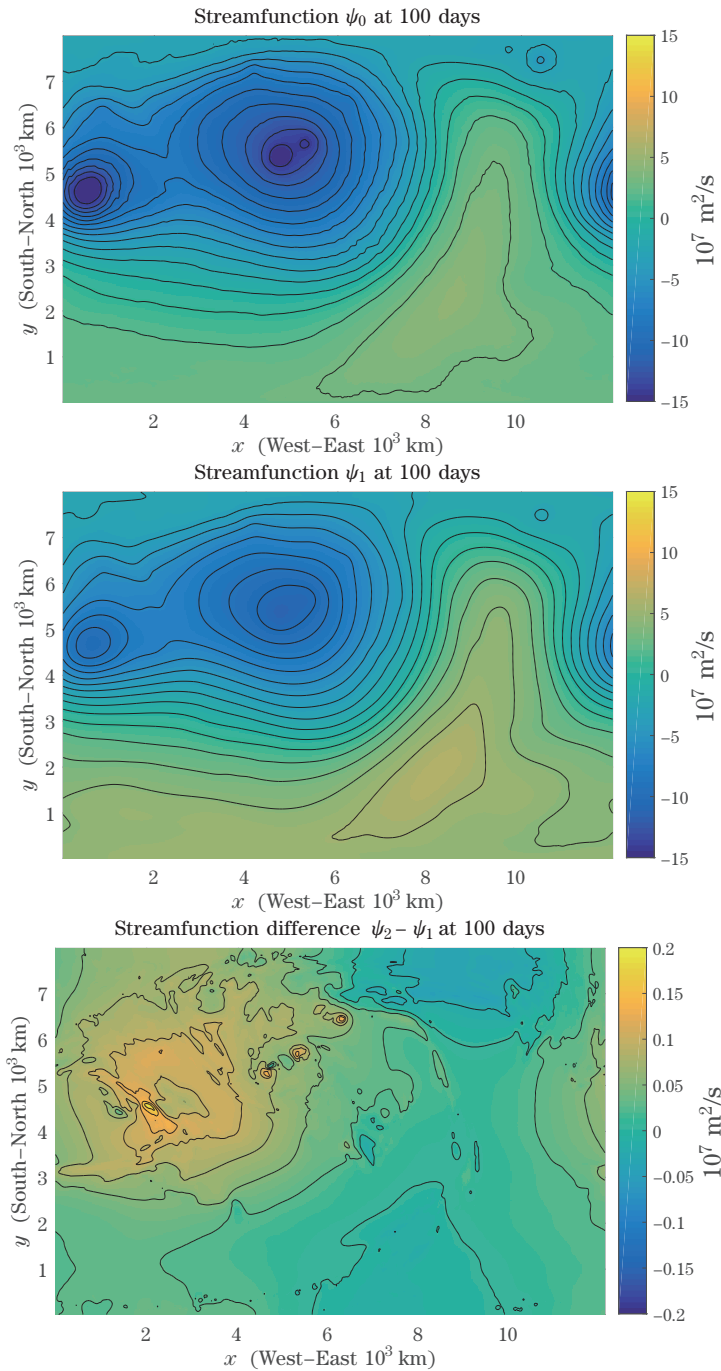


Figure 11 Balanced streamfunction obtained using the three methods described in Section 3 at 4 km height and 100 days after start of simulation. Black lines are streamfunction level sets or streamlines for the balanced flow. Top: Streamfunction estimate from pressure  $\psi_0$ . Middle: One phase streamfunction  $\psi_1$ . Bottom: Difference between two and one phase streamfunctions  $\psi_2 - \psi_1$ .

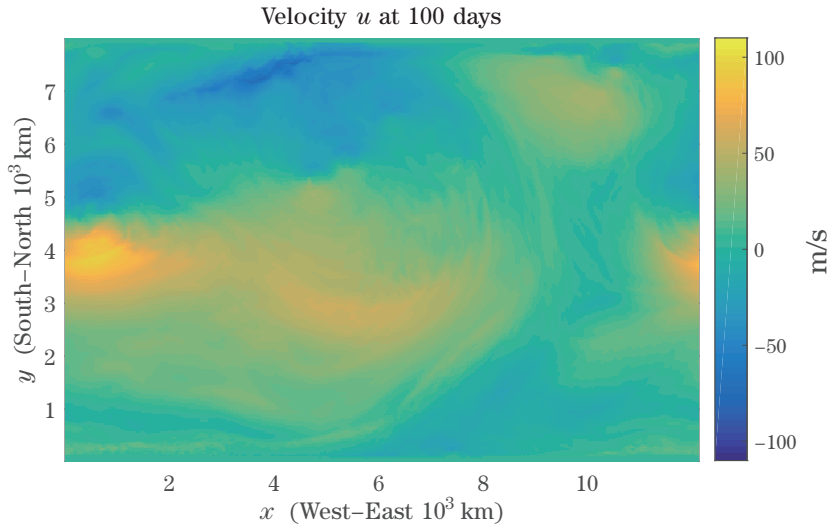


Figure 12 Velocity from simulation at 4 km height 100 days after start of simulation.

Moreover, the one and two phase velocities differ from each other at scales below  $\approx 400$  km; the scales associated with the cloud water, as seen in Figure 10.

We may similarly compare cross-sections of the potential temperature with the balanced temperature at the 4 km height. We show the temperature in Figure 14 and temperature differences, the unbalanced temperatures, in Figure 15. We find that the potential temperature  $\theta$  is approximated very well by the balanced solutions for large scales. Indeed,  $\|\theta - \theta_0\|_2 / \|\theta\|_2 \approx 0.2134$ ,  $\|\theta - \theta_1\|_2 / \|\theta\|_2 \approx 0.0919$ , and  $\|\theta_2 - \theta_1\|_2 / \|\theta_1\|_2 \approx 0.0167$ . So, while the estimate from pressure  $\theta_0$  still differs significantly from the one and two phase temperatures, they all collectively match the raw temperature broadly. In addition, the one and two phase balanced temperature variables are again very close (2%) to each other in the large scale sense.

To observe the small scale features that are filtered out by the balanced temperatures we show the temperature differences in Figure 15. We see that the differences between the raw potential temperature  $\theta$  and the balanced temperature  $\theta_0$  are broadly in the large scale and mostly of the order of 5 K. The difference between the raw temperature  $\theta$  and the balanced one phase temperature  $\theta_1$  and two phase temperature  $\theta_2$  are mostly in the small scale (below  $\approx 500$  km) and have significant amplitude differences of 15 K. The locations where these differences between the one and two phase solution and the raw data occur coincide with the location of the strong streamfunction vortices of Figure 11 and the cloud water shown in Figure 10. In addition, the differences between one and two phase balanced temperatures are significant (order of 5 K), match very closely the cloud water distribution, and are most prominent in the location of the two vortices; the fact that the difference between one and two phase streamfunctions are most significant in regions with cloud water is consistent with our discussion in Section 4.4.

We consider once more the mean in the  $y$  direction of the magnitude of the Fourier transform

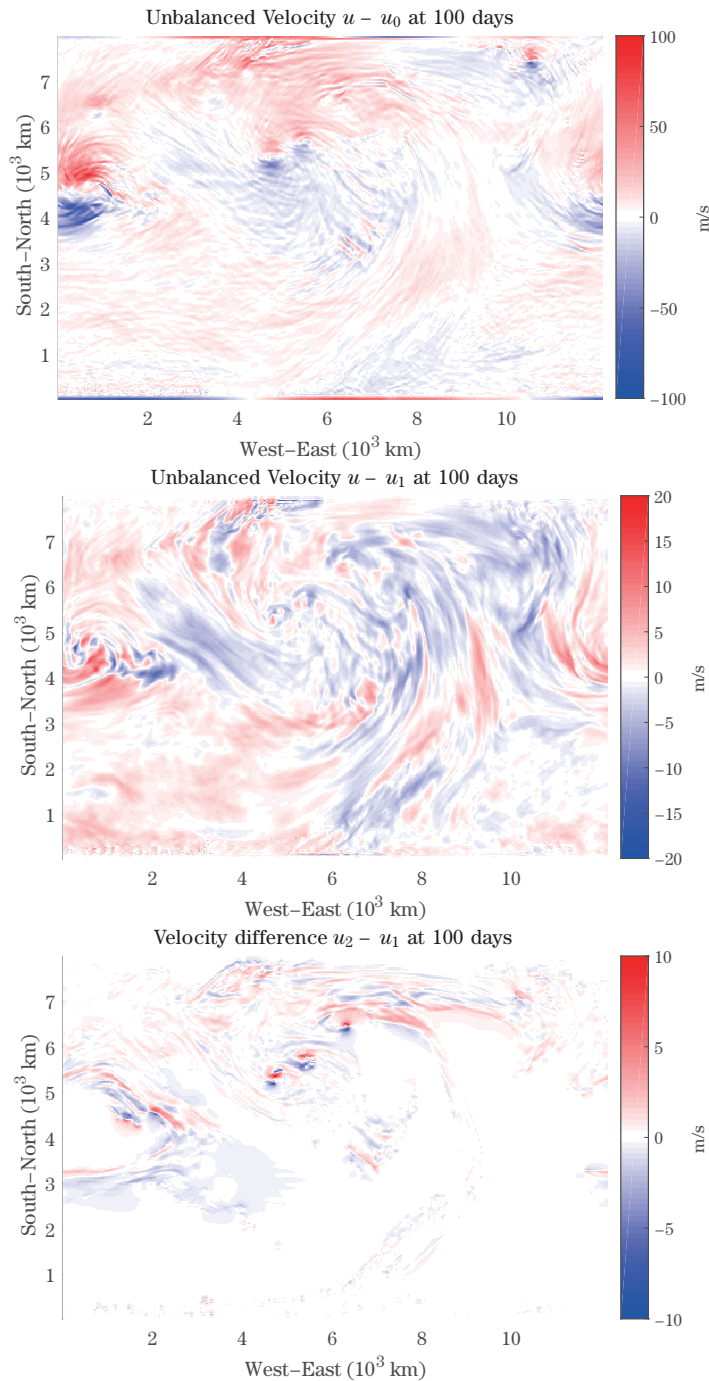


Figure 13 Comparison of velocity with the balanced velocities obtained from the three methods of Section 3 at 4 km height and 100 days. Top: Difference between velocity and balanced velocity from pressure. Middle: Difference between velocity and balanced velocity from one phase streamfunction. Bottom: Difference between balanced velocities from two and one phase streamfunctions.

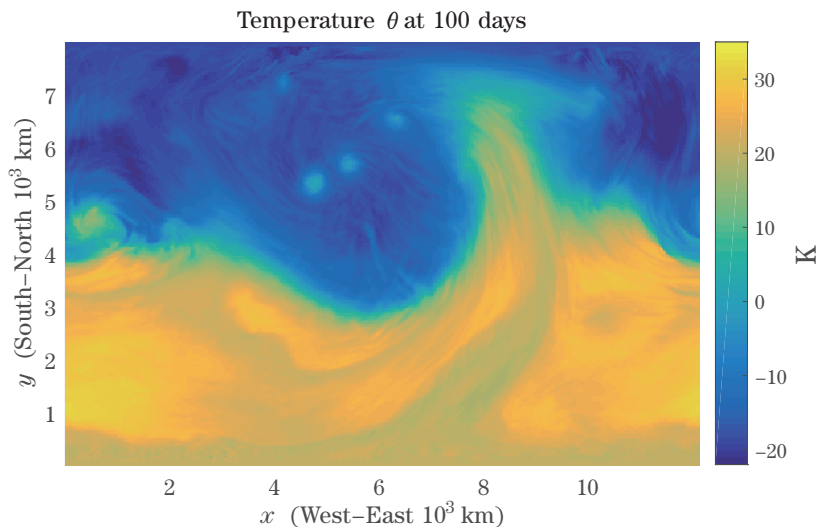


Figure 14 Temperature from simulation at 4 km height 100 days after start of simulation.

in the  $x$  direction for a fixed  $z = 4$  km and show these results for the temperature in the right plot of Figure 16. We find that this plot broadly corroborates our conclusions so far, but allows us to quantify our observations. Namely, we find that the potential temperature  $\theta$  and the balanced potential temperature arising from the pressure  $\theta_0$  are nearly indistinguishable at all scales. The one and two phase balanced temperatures begin to differ from the potential temperature at about the  $\approx 1000$  km scale and begin to differ from each other below  $\approx 400$  km. Thus, the one and two phase balanced temperatures filter out the small scale features of the temperature and differ between each other at the scales associated with the cloud water content of the flow.

## 6 Conclusion

We have presented a procedure to determine the balanced and unbalanced components of atmospheric variables in moist mid-latitude flows. To accomplish this, we were motivated by the anelastic PQG equations [43] with the three moisture constituents of water vapor, cloud water, and rainwater. These equations give rise to a natural decomposition of balanced and unbalanced modes by means of a PV and moisture variable (M) inversion that recovers the QG streamfunction of this moist problem under suitable boundary conditions. This inversion procedure differs from those previously considered in the recognition that both PV and M variables—accounting for moisture, precipitation, and two phases of water—are necessary to recover the streamfunction, rather than a single dry PV variable. This QG streamfunction may then be used to construct all other balanced variables of the system, including balanced moisture variables.

To recover the streamfunction, we considered three methods: using the pressure as a proxy

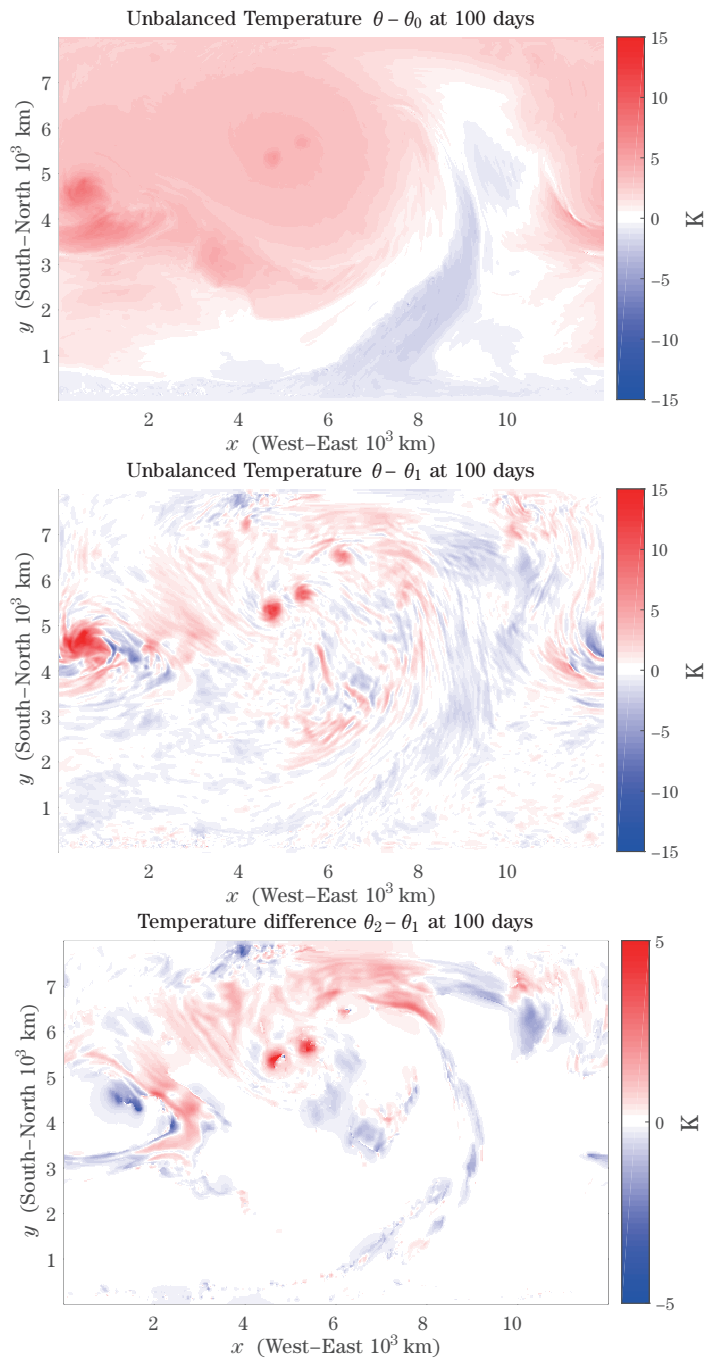


Figure 15 Differences between temperature  $\theta$  and balanced temperatures  $\theta_i$  for  $i = 0, 1, 2$  obtained from the three methods of Section 3 at 4 km height at 100 days.

for the streamfunction, a one phase PV-and-M inversion, or a two phase PV-and-M inversion. The streamfunction recovered from each method leads to balanced variables that broadly capture the large scale, synoptic features of the atmospheric quantity in question. Namely, the

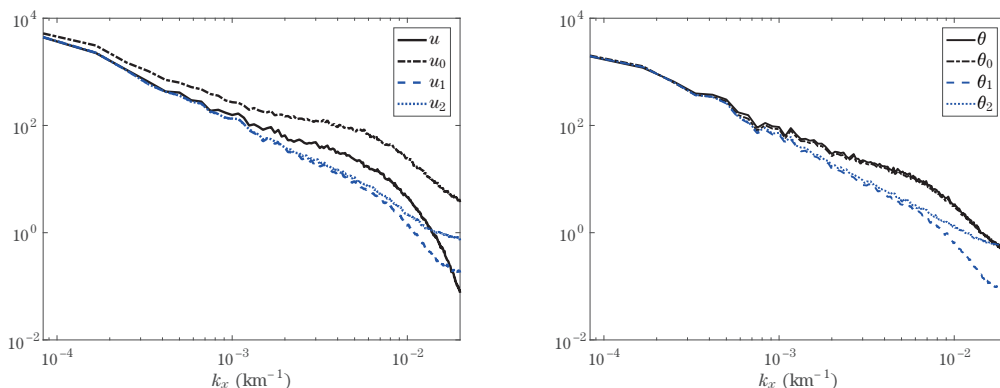


Figure 16 Mean in  $y$  (meridional) direction of magnitude of Fourier transforms in the  $x$  (zonal) direction at 4 km height and 100 days. Left: Velocity. Right: Potential temperature. The raw potential temperature  $\theta$  and the balanced temperature  $\theta_0$  are nearly identical on the right-hand picture.

balanced components of both velocity and temperature capture the large scale features of the raw velocity and temperature. Of the three methods, the balanced components arising from pressure do worst in capturing the large scale features of the flow. The balanced variables, however, mainly differ from each other and the raw data at smaller scales associated with the phase transitions and the cloud water. Therefore, considerable differences may arise between solutions of different inversion procedures.

The main finding is that it is within the cloud where the two-phase inversion method has the most substantial differences from the one-phase inversion method. For example, within the cloud, the potential temperature difference of the two methods,  $\theta_1 - \theta_2$ , is as large as 5 K. Furthermore, a theoretical explanation was derived in (4.7) in the form of an elliptic PDE for the difference  $\psi_1 - \psi_2$  in the one-phase and two-phase streamfunctions. The forcing in the elliptic PDE is related to the cloud water,  $q_c$ , the presence of cloud water is a main factor in creating differences between the different inversion methods. Another key factor is that the two-phase inversion involves two different buoyancy frequencies,  $N_u^2$  and  $N_s^2$ , corresponding to the unsaturated and saturated phases, respectively; and the different values of  $N_u^2$  and  $N_s^2$  contribute to the differences seen in the streamfunctions  $\psi_1$  and  $\psi_2$ .

Lastly, we note that one may similarly consider the effects that the different inversion procedures have on the balanced component of total water. In particular, it may be of interest to determine the dependence of the balanced component of moisture on features arising from the moisture such as the phase transition and rainwater. We leave, however, the analysis of this quantity for a future paper.

## References

- [1] Bannon, P. R., On the anelastic approximation for a compressible atmosphere, *J. Atmos. Sci.*, **53**(23), 1996, 3618–3628.
- [2] Derber, J. and Bouttier, F., A reformulation of the background error covariance in the ECMWF global data assimilation system, *Tellus A*, **51**(2), 1999, 195–221.
- [3] Dutrifoy, A. and Majda, A. J., The dynamics of equatorial long waves: a singular limit with fast variable coefficients, *Commun. Math. Sci.*, **4**(2), 2006, 375–397.
- [4] Dutrifoy, A. and Majda, A. J., Fast wave averaging for the equatorial shallow water equations, *Comm. PDEs*, **32**(10), 2007, 1617–1642.
- [5] Dutrifoy, A. and Majda, A. J. and Schochet, S., A simple justification of the singular limit for equatorial shallow-water dynamics, *Comm. Pure Appl. Math.*, **62**(3), 2009, 322–333.
- [6] Emanuel, K. A., Atmospheric Convection, Oxford University Press, New York, 1994.
- [7] Embid, P. F. and Majda, A. J., Averaging over fast gravity waves for geophysical flows with arbitrary potential vorticity, *Comm. PDEs*, **21**(3–4), 1996, 619–658.
- [8] Embid, P. F. and Majda, A. J., Low Froude number limiting dynamics for stably stratified flow with small or finite Rossby numbers, *Geophys. Astrophys. Fluid Dynam.*, **87**(1–2), 1998, 1–50.
- [9] Fogelson, A. L. and Keener, J. P., Immersed interface methods for Neumann and related problems in two and three dimensions, *SIAM J. Sci. Comput.*, **22**(5), 2001, 1630–1654.
- [10] Frierson, D. M. W. and Majda, A. J. and Pauluis, O. M., Large scale dynamics of precipitation fronts in the tropical atmosphere: a novel relaxation limit, *Commun. Math. Sci.*, **2**(4), 2004, 591–626.
- [11] Grabowski, W. W. and Smolarkiewicz, P. K., Two-time-level semi-Lagrangian modeling of precipitating clouds, *Mon. Wea. Rev.*, **124**(3), 1996, 487–497.
- [12] Hernandez-Duenas, G., Majda, A. J., Smith, L. M. and Stechmann, S. N., Minimal models for precipitating turbulent convection, *J. Fluid Mech.*, **717**, 2013, 576–611.
- [13] Hoskins, B. J., McIntyre, M. E. and Robertson, A. W., On the use and significance of isentropic potential vorticity maps, *Q. J. Roy. Met. Soc.*, **111**(470), 1985, 877–946.
- [14] Kalnay, E., Atmospheric modeling, data assimilation and predictability, Cambridge University Press, Cambridge, 2003.
- [15] Kessler, E., On the distribution and continuity of water substance in atmospheric circulations, Number 32 in Meteorological Monographs. American Meteorological Society, Providence, 1969.
- [16] Khouider, B., Majda, A. J. and Stechmann, S. N., Climate science in the tropics: waves, vortices and PDEs, *Nonlinearity*, **26**(1), 2013, R1–R68.
- [17] Klainerman, S. and Majda, A. J., Singular limits of quasilinear hyperbolic systems with large parameters and the incompressible limit of compressible fluids, *Comm. Pure Appl. Math.*, **34**(4), 1981, 481–524.
- [18] Klainerman, S. and Majda, A. J., Compressible and incompressible fluids, *Comm. Pure Appl. Math.*, **35**(5), 1982, 629–651.
- [19] Klein, R. and Majda, A. J., Systematic multiscale models for deep convection on mesoscales, *Theor. Comp. Fluid Dyn.*, **20**(5–6), 2006, 525–551.
- [20] Kleist, D. T., Parrish, D. F., Derber, J. C., Treadon, R., Errico, R. M. and Yang, R., Improving incremental balance in the GSI 3DVAR analysis system, *Mon. Wea. Rev.*, **137**(3), 2009, 1046–1060.
- [21] Lackmann, G., Midlatitude Synoptic Meteorology: Dynamics, Analysis, and Forecasting, American Meteorological Society, Providence, 2011.
- [22] LeVeque, R. J., Finite Difference Methods for Ordinary and Partial Differential Equations, Steady State and Time Dependent Problems, Society for Industrial and Applied Mathematics (SIAM), Philadelphia, 2007.
- [23] LeVeque, R. J. and Li, Z., The immersed interface method for elliptic equations with discontinuous coefficients and singular sources, *SIAM J. Numer. Anal.*, **31**(4), 1994, 1019–1044.
- [24] Li, Z., A note on immersed interface method for three-dimensional elliptic equations, *Comput. Math. Appl.*, **31**(3), 1996, 9–17.
- [25] Li, Z. and Ito, K., Maximum principle preserving schemes for interface problems with discontinuous coefficients, *SIAM J. Sci. Comput.*, **23**(1), 2001, 339–361.
- [26] Lipps, F. B., Hemler, R. S., A scale analysis of deep moist convection and some related numerical calculations, *J. Atmos. Sci.*, **39**(10), 1982, 2192–2210.

- [27] Liu, X.-D. and Fedkiw, R. P. and Kang, M., A boundary condition capturing method for Poisson's equation on irregular domains, *J. Comput. Phys.*, **160**(1), 2000, 151–178.
- [28] Liu, X.-D. and Sideris, T., Convergence of the ghost fluid method for elliptic equations with interfaces, *Math. Comput.*, **72**(244), 2003, 1731–1746.
- [29] Majda, A. J., Compressible Fluid Flow and Systems of Conservation Laws in Several Space Variables, volume 53 of Applied Mathematical Sciences, Springer-Verlag, New York, 1984.
- [30] Majda, A. J., Introduction to PDEs and Waves for the Atmosphere and Ocean, Volume 9 of Courant Lecture Notes in Mathematics, American Mathematical Society, Providence, 2003.
- [31] Majda, A. J. and Embid, P., Averaging over fast gravity waves for geophysical flows with unbalanced initial data, *Theor. Comput. Fluid Dyn.*, **11**(3–4), 1998, 155–169.
- [32] Majda, A. J. and Harlim, J., Filtering Turbulent Complex Systems, Cambridge University Press, Cambridge, 2012.
- [33] Majda, A. J. and Klein, R., Systematic multiscale models for the Tropics, *J. Atmos. Sci.*, **60**(2), 2003, 393–408.
- [34] Majda, A. J. and Souganidis, P. E., Existence and uniqueness of weak solutions for precipitation fronts: A novel hyperbolic free boundary problem in several space variables, *Comm. Pure Appl. Math.*, **63**(10), 2010, 1351–1361.
- [35] Marshall, J. and Plumb, R. A., Atmosphere, Ocean, and Climate Dynamics: An Introductory Text, Academic Press, Boston, MA, 2007.
- [36] Martin, J. E., Mid-latitude Atmospheric Dynamics: A First Course, John Wiley & Sons, Chichester, 2006.
- [37] McTaggart-Cowan, R., Gyakum, J. R. and Yau, M. K., Moist component potential vorticity, *J. Atmos. Sci.*, **60**(1), 2003, 166–177.
- [38] Ogura, Y. and Phillips, N. A., Scale analysis of deep and shallow convection in the atmosphere, *J. Atmos. Sci.*, **19**(2), 1962, 173–179.
- [39] Parrish, D. F. and Derber, J. C., The National Meteorological Center's spectral statistical-interpolation analysis system, *Mon. Wea. Rev.*, **120**(8), 1992, 1747–1763.
- [40] Rogers, R. R. and Yau, M. K., A Short Course in Cloud Physics, Butterworth–Heinemann, Burlington, 1989.
- [41] Schubert, W. H., Hausman, S. A., Garcia, M., Ooyama, K. V. and Kuo, H.-C., Potential vorticity in a moist atmosphere, *J. Atmos. Sci.*, **58**(21), 2001, 3148–3157.
- [42] Skamarock, W. C., Klemp, J. B., Dudhia, J., Gill, D. O., Barker, D. M., Duda, M. G., Huang, X.-Y., Wang, W. and Powers, J. G., A description of the Advanced Research WRF Version 3, NCAR/TN–475+STR, NCAR, 2008.
- [43] Smith, L. M. and Stechmann, S. N., Precipitating quasigeostrophic equations and potential vorticity inversion with phase changes, *J. Atmos. Sci.*, **74**(10), 2017, 3285–3303.
- [44] Stechmann, S. N. and Majda, A. J., The structure of precipitation fronts for finite relaxation time, *Theor. Comp. Fluid Dyn.*, **20**(5–6), 2006, 377–404.
- [45] Stevens, B., Atmospheric moist convection, *Annu. Rev. Earth Planet. Sci.*, **33**(1), 2005, 605–643.
- [46] Trefethen, L. N. and Bau III, D., Numerical Linear Algebra, Society for Industrial and Applied Mathematics (SIAM), Philadelphia, 1997.
- [47] Tzou, C.-N. and Stechmann, S. N., Simple second-order finite differences for elliptic PDEs with discontinuous coefficients and interfaces, *Comm. App. Math. and Comp. Sci.*, **14**(2), 2019, 121–147.
- [48] Vallis, G. K., Atmospheric and Oceanic Fluid Dynamics: Fundamentals and Large-scale Circulation, Cambridge University Press, New York, 2006.
- [49] Wetzel, A. N., Smith, L. M. and Stechmann, S. N., Moisture transport due to baroclinic waves: Linear analysis of precipitating quasi-geostrophic dynamics, *Math. Clim. Weather Forecast.*, **3**(1), 2017, 28–50.
- [50] Zhou, Y.-S. and Zhu, K.-F. and Zhang, Z., Anomaly of the moist potential vorticity substance with mass forcing and its application in diagnosing Mei-yu front rainfall, *Atmos. Ocean. Sci. Lett.*, **8**(1), 2015, 39–44.